

Nonlinear instability of elementary stratified flows at large Richardson number

Andrew J. Majda^{a)}

Courant Institute of Mathematical Sciences, New York University, 251 Mercer Street, New York, New York 10012-1185

Michael G. Shefter

Courant Institute of Mathematical Sciences, New York University, 251 Mercer Street, New York, New York 10012-1185

(Received 3 March 1999; accepted for publication 15 April 1999)

Elementary stably stratified flows with linear instability at all large Richardson numbers have been introduced recently by the authors [J. Fluid Mech. **376**, 319–350 (1998)]. These elementary stratified flows have spatially constant but time varying gradients for velocity and density. Here the nonlinear stability of such flows in two space dimensions is studied through a combination of numerical simulations and theory. The elementary flows that are linearly unstable at large Richardson numbers are purely vortical flows; here it is established that from random initial data, linearized instability spontaneously generates local shears on buoyancy time scales near a specific angle of inclination that nonlinearly saturates into localized regions of strong mixing with density overturning resembling Kelvin–Helmholtz instability. It is also established here that the phase of these unstable waves does not satisfy the dispersion relation of linear gravity waves. The vortical flows are one family of stably stratified flows with uniform shear layers at the other extreme and elementary stably stratified flows with a mixture of vorticity and strain exhibiting behavior between these two extremes. The concept of effective shear is introduced for these general elementary flows; for each large Richardson number there is a critical effective shear with strong nonlinear instability, density overturning, and mixing for elementary flows with effective shear below this critical value. The analysis is facilitated by rewriting the equations for nonlinear perturbations in vorticity-stream form in a mean Lagrangian reference frame. © 2000 American Institute of Physics. [S1054-1500(00)00801-6]

The issue of stability of large scale stratified flows plays an essential role both for theoretical and practical reasons, in particular, in designing numerical models for stratified turbulence. This work discusses stability properties of several classes of elementary time periodic flows with density stratification parametrized by the Richardson number. An important analytical result, due to Miles and Howard, establishes that stationary shear flows with the Richardson number higher than a specified threshold value are stable to small perturbations. This result is often utilized by various numerical models of turbulence for switching off the turbulent diffusivity when the Richardson number is large, even in situations where the Miles–Howard criterion is formally not applicable. We present several unambiguous elementary examples of time periodic flows with instabilities in the fully nonlinear regime. To better characterize the stability properties of the elementary flows, in addition to the Richardson number we introduce the effective shear associated with the net shearing effect of the elementary flows over one period.

^{a)}Author to whom correspondence should be addressed: Electronic mail: kronhaus@cims.nyu.edu

I. INTRODUCTION

The nature of instabilities, mixing and turbulence in stably stratified flows is important for flows in the atmosphere and ocean which often have stable density gradients as well as for a variety of engineering flows.^{1,2} In general, mixing and turbulence are suppressed in stably stratified flows at high Richardson numbers when compared with homogeneous turbulent flows;^{1,2} nevertheless, the instability and mixing that occurs can have a significant effect on larger scale motion and the parametrization of these effects in numerical models is an important practical issue.^{2,3,4}

The Miles–Howard theorem suggests that shear instability is suppressed with strong stratification.^{5,6} This theorem states that steady shear flows $\vec{V}=(v(z),0,0)$ in an inviscid stably stratified fluid are linearly stable for all Richardson numbers, Ri , satisfying

$$Ri > \frac{1}{4}, \quad Ri = \frac{N^2}{\left(\frac{\partial v}{\partial z}\right)^2} \quad (1)$$

with $N^2 = -g \partial \rho / \partial z / \rho_0$, the square of the buoyancy or Brunt–Vaisala frequency. The criterion in (1) is often interpreted and applied literally for time-dependent flow fields in numerical modeling for the atmosphere or ocean. For example, a popular turbulent eddy diffusivity used in numerical

simulations in the atmosphere/ocean community is the Lilly–Smagorinsky eddy diffusivity^{7,8} where the turbulent eddy diffusivity is completely switched off and set to zero for $Ri \geq \overline{Ri} \geq \frac{1}{4}$ with \overline{Ri} of order unity.^{3,4,9}

In contrast to the above viewpoint, important theoretical work of Drazin¹⁰ demonstrates that a monochromatic propagating gravity wave in a stably stratified flow is unstable at all Richardson numbers and recent numerical simulations¹¹ reveal that such instabilities lead to breaking gravity waves with subsequent nonlinear mixing at moderately large Richardson numbers. Recently the authors¹² have introduced a class of elementary time-dependent stably stratified flows and have demonstrated that these flows are linearly unstable in three dimensions at all large Richardson numbers. The dominant linearized instabilities in these flows are purely two-dimensional parametric instabilities which grow at twice the period of the underlying elementary flow.¹² These elementary flows have constant spatial gradients for both velocity and density which vary in time. Parametric instabilities are often found in the behavior of internal gravity waves. One prominent example is the pioneering work of Orlandi¹³ where parametric instabilities arise simply through time-periodic variations in the buoyancy frequency. In contrast, the basic states studied here involve self-consistent nonlinear interaction through baroclinic vorticity production.

The elementary flows with instability at all large Richardson numbers are purely vortical flows with time-dependent dynamics described by the nonlinear pendulum equation¹² (see Sec. II). These vortical flows are one extreme case of elementary stratified flows introduced in Ref. 12 with uniform shear layers at the other extreme as well as other more general elementary flows with a combination of vorticity and strain (see Sec. II) with intermediate behavior between these two extreme cases. Such elementary flows are motivated by the general kinematic fact following directly from Taylor expansion that every stratified flow field locally has constant velocity and density gradients with high accuracy. Thus, general solutions of the time-dependent Boussinesq equations with spatially constant but time varying gradients provide a local fit to more general stratified fluid motions.^{12,14,15} Therefore, the smaller scale nonlinear instabilities which occur in such elementary flows can provide fundamental insight into the subtle issues of mixing at large Richardson numbers for more general flows as well as their sub-grid scale parametrization.

The goal of this paper is to study the nonlinear instability, density overturning, and mixing in perturbations of the elementary stratified flows described above. Here we focus on the nonlinear development of instabilities within the inviscid Boussinesq equations in two space variables. We do this for two reasons: the dominant modes of linearized instability are purely two dimensional;¹² in two dimensions, we exploit the vorticity-stream formulation of the Boussinesq equations and mean Lagrangian coordinates (Sec. II C) to obtain an elegant reformulation of both the linear and nonlinear instability of elementary flows which is transparent for the study of both linear and nonlinear stability.

In Sec. II, we describe the elementary exact solutions of the Boussinesq equations which provide the basic states in

our study of nonlinear instability. We also introduce the important concept of effective shear for elementary flows which plays a crucial role for interpreting the results in subsequent sections of the paper. We end Sec. II with the reformulation utilizing mean Lagrangian coordinates. In Sec. III, we briefly summarize a transparent linear stability theory in mean Lagrangian coordinates; these results play a crucial role in designing and interpreting the numerical experiments for nonlinear stability theory in subsequent sections. We also establish that the basic instabilities for elementary vortical flows at large Richardson numbers have a phase speed which is fundamentally different than propagating linear gravity waves. In Sec. IV, we show that small amplitude random perturbations of the purely vortical flows at large Richardson numbers excite linear instabilities on buoyancy time scales which saturate through nonlinear interaction into local unstable shear flows with significant mixing and density overturning, resembling Kelvin–Helmholtz instability. In Sec. V, we briefly discuss shear flow perturbations and establish that the kinetic energy of perturbations can amplify in a transient phase to similar amplitudes as in the earlier situation with purely vortical flows but without significant transfer to the potential energy in the perturbed flow and without any overturning of density or mixing. In Sec. VI, we study the nonlinear instability for elementary fluid flows with behavior between the two extreme cases described in Secs. IV and V. Here the concept of effective shear introduced in Sec. II is important for interpreting the results: nonlinear perturbations of the elementary flows with effective shear below a critical threshold behave like the vortical flows from Sec. IV at large Richardson numbers while perturbations of those flows above the effective shear threshold behave like the shear flow perturbations discussed in Sec. V.

II. ELEMENTARY EXACT SOLUTIONS AND THEIR PERTURBATIONS

A. Boussinesq equations and vorticity-stream formulation

In this paper we study stability properties of elementary stratified flows, satisfying the nondimensional Boussinesq equations in the absence of viscosity and heat conduction:

$$\begin{aligned} \frac{D\vec{v}}{Dt} &= -\nabla p - \rho \vec{e}_3, \\ \text{div } \vec{v} &= 0, \\ \frac{D\rho}{Dt} &= 0. \end{aligned} \tag{2}$$

The nondimensional units are presented below in (8). Here, we restrict our consideration to purely two-dimensional flows where $\vec{v}(x,z,t) = (u(x,z,t), w(x,z,t))^T$ are two-dimensional velocity fields, with no dependence on the horizontal direction y . In (2), $\rho(x,z,t)$ is the total nondimensional flow density and p is the nondimensional hydrodynamic pressure. The details of the nondimensionalization procedure are sketched below in (8). For such two-dimensional flows, the Boussinesq equations in (2) allow a simple vorticity-stream formulation, with vorticity

$$\Omega(x, z, t) = \frac{\partial u}{\partial z} - \frac{\partial w}{\partial x}$$

and the stream function $\psi(x, z, t)$, introduced via

$$\vec{v} = \nabla^\perp \psi = \begin{pmatrix} \partial_z \psi \\ -\partial_x \psi \end{pmatrix}. \tag{3}$$

The incompressibility constraint $u_x + w_z = 0$ is satisfied trivially, provided that (3) holds. A simple calculation shows the Eqs. in (2) take the form,

$$\begin{aligned} \Omega_t + \nabla^\perp \psi \cdot \nabla \Omega &= \rho_x, \\ \rho_t + \nabla^\perp \psi \cdot \nabla \rho &= 0, \\ \Delta_2 \psi &= \Omega. \end{aligned} \tag{4}$$

B. Elementary flows and exact solutions

The equations in (2) or, equivalently, in (4) have an interesting family of elementary solutions.^{12,14} The velocity and density fields in these elementary solutions have a linear structure in space, with the vorticity depending on time only. Such flows have a simple physical interpretation and should be viewed as local Taylor expansions of general flows. In this study we will use the following family of elementary flows:

$$\begin{aligned} \vec{\Omega}(t) &= \bar{\omega}(t) \vec{e}_2, \quad \rho = \rho_b + b_1(t)x + b_3(t)z, \\ \vec{v} &= \left(\frac{\bar{\omega}(t) + \sigma}{2} z, -\frac{\bar{\omega}(t) + \sigma}{2} x \right). \end{aligned} \tag{5}$$

Here, σ is the background (constant) strain rate, $\bar{\omega}(t)$ is the only component of spatially constant vorticity, and $b_1(t)$ and $b_3(t)$ are the horizontal and vertical density gradients. The system in (4) reduces to the system of three ordinary differential equations¹² for the elementary flows in (5)

$$\begin{aligned} \frac{d\bar{\omega}}{dt} &= b_1, \\ \frac{db_1}{dt} &= \frac{-\sigma + \bar{\omega}}{2} b_3, \\ \frac{db_3}{dt} &= -\frac{\sigma + \bar{\omega}}{2} b_1. \end{aligned} \tag{6}$$

An appropriate set of initial conditions is given by a nonzero value of vorticity and stable vertical stratification in the density field:

$$\bar{\omega}(0) = \bar{\omega}_0, \quad b_1(0) = 0, \quad b_3(0) = -B_0, \quad B_0 > 0. \tag{7}$$

The nondimensionalization procedure for (2) which we utilize here involves the ambient density ρ_b , an initial value of vertical stratification B_0 , and gravity g as basic scales. The nondimensional form for the variables involved in Eqs. (2) and (4) is given by

$$\begin{aligned} \vec{x} &\rightarrow \frac{\rho_b}{B_0} \vec{\tilde{x}}, \quad t \rightarrow \frac{\tilde{t}}{\mathcal{N}}, \quad b \rightarrow B_0 \tilde{b}, \quad \bar{\omega} \rightarrow \mathcal{N} \tilde{\bar{\omega}}, \\ \sigma &\rightarrow \mathcal{N} \tilde{\sigma}, \quad \vec{v} \rightarrow \frac{\mathcal{N} \rho_b}{B_0} \tilde{v}, \quad \rho \rightarrow \rho_b \tilde{\rho}, \end{aligned} \tag{8}$$

in terms of the two nondimensional numbers,

$$\mathcal{N}^2 = \frac{gB_0}{\rho_b}, \quad Fr = \frac{\bar{\omega}_0}{\mathcal{N}}.$$

Here, \mathcal{N} is the Brunt–Vaisala buoyancy frequency and Fr is the Froude number associated with this flow. Since only non-dimensional variables will be used throughout the rest of this paper, we will drop the tildes at this point. Clearly, the equations in (6) have an identical form in nondimensional variables; the initial conditions in (7) become

$$\bar{\omega}(0) = Fr, \quad b_1(0) = 0, \quad b_3(0) = -1. \tag{9}$$

A crucially important characterization of stratified flows is given by the Richardson number, relating the time scales associated with stratification and large eddy motions. For the time-dependent flows in (5), the authors¹² introduced the following natural definition of the Richardson number:

$$\mathcal{R}i = \min_t Ri(t) = \min_t \left[\frac{\mathcal{N}^2(t)}{\bar{\omega}^2(t) + \sigma^2/2} \right]. \tag{10}$$

The Richardson number defined above is always smaller than the conventional Richardson number, $Ri = \mathcal{N}^2 / (\partial \vec{v}_H / \partial z)^2$, and, thus, provides a more conservative choice for stability studies.

In this paper we will inquire about the nonlinear stability of three types of elementary flows in (5). First, we study purely vortical flows, with $\sigma = 0$. The flow parameters $\bar{\omega}(t), b_1(t), b_3(t)$ are periodic functions, with the density and velocity of the form

$$\rho = 1 + \sin \theta(t)x - \cos \theta(t)z, \quad \vec{v} = \left(\frac{\bar{\omega}(t)}{2} z, -\frac{\bar{\omega}(t)}{2} x \right).$$

A direct calculation yields that the vorticity $\bar{\omega}(t)$ is related to the phase function $\theta(t)$ that satisfies the nonlinear pendulum equation

$$\bar{\omega}(t) = -2 \frac{d\theta}{dt}, \quad 2 \frac{d^2\theta}{dt^2} = -\sin \theta(t), \tag{11}$$

with the initial data

$$\theta(t)|_{t=0} = 0, \quad \bar{\omega}(t)|_{t=0} = (\mathcal{R}i)^{-1/2}. \tag{12}$$

The authors¹² showed that flows with $\mathcal{R}i < 1/4$ present no overturning, while flows with $\mathcal{R}i > 1/4$ always overturn, in rough agreement with the Miles–Howard theorem.^{5,6}

The next important type of elementary solutions are shear flows, expressed by equilibrium points of the equations in (6). There, vorticity balances strain exactly so that the flow parameters remain equal to their initial values,

$$b_1(t) \equiv 0, \quad b_3(t) \equiv -1, \quad \bar{\omega}(t) \equiv Fr, \tag{13}$$

and the velocity field $\vec{v} = ((Fr)z, 0)$ is the vertical shear of horizontal velocity, justifying the name for this type of flow.

Finally, we will study stability of general flows in (5), with no implied special conditions for $\bar{\omega}$ and σ . The flow parameters $\bar{\omega}(t)$, $b_1(t)$, and $b_3(t)$ are periodic functions of time; their evolution is described by a Hamiltonian and equivalent to motion of a particle in a quartic potential well.¹² If the strain flow associated with σ is not aligned exactly at an angle of 45°, then either $Ri(t) \rightarrow 0$ or $Ri(t) \rightarrow \infty$ rapidly in time; for these reasons, we will not discuss these flows further. Here we do not elaborate on details of the derivation.¹² For the vortical flows and shear flows our conservative definition of Richardson number is related to the classical value in (1) by $Ri = 4\mathcal{R}i$ (in the nonoverturning regime, with $\mathcal{R}i > 1/4$) and $Ri = 1.5\mathcal{R}i$, and for general flows, all values between these two extremes.

C. Perturbations and mean Lagrangian coordinates

In the previous two sections we discussed the construction of elementary exact solutions to the inviscid Boussinesq equations, written in the vorticity-stream form for two-dimensional flows. Here we derive the equations to describe perturbations of elementary flows. Also, at the end of the section, we will introduce the important notion of effective shear, that arises naturally for elementary flows.

We start by introducing the following decomposition of the velocity, vorticity, and density fields,

$$\begin{aligned} \vec{\Omega}(x, z, t) &= (\bar{\omega}(t) + \omega'(x, z, t))\vec{e}_2, \\ \vec{v}(x, z, t) &= \vec{V}(x, z, t) + \vec{v}'(x, z, t), \\ \bar{\rho}(x, z, t) &= \bar{\rho}(x, z, t) + \rho'(x, z, t), \end{aligned}$$

where $\bar{\omega}(t)$, $\vec{V}(x, z, t)$, and $\bar{\rho}(x, z, t) = 1 + b_1(t)x + b_3(t)z$ represent an elementary solution and the primed variables denote perturbations. To simplify the notation, we neglect the primes and rewrite the equations in (4) for perturbation variables,

$$\begin{aligned} \omega_t + \vec{V} \cdot \nabla \omega + (\nabla^\perp \psi \cdot \nabla \omega) &= \rho_x, \\ \rho_t + \vec{V} \cdot \nabla \rho + (\nabla^\perp \psi \cdot \nabla \rho) + (\nabla^\perp \psi \cdot \nabla \bar{\rho}) &= 0, \\ \Delta \psi &= \omega, \end{aligned} \tag{14}$$

where ψ is the perturbation stream function. With the nondimensional variables introduced in (8) in Sec. II B, the initial conditions take the following scaled form:

$$\begin{aligned} \Omega(0) &= Fr(1 + \omega(x, z, t))|_{t=0}, \\ \bar{\rho}(0) &= 1 - z + Fr \rho(x, z, t)|_{t=0}. \end{aligned}$$

The equations in (14) assume a more elegant and computationally convenient form when written in Lagrangian coordinates associated with the mean flow. If we denote Eulerian coordinates by $\vec{\mathcal{X}} = (x, z)$ and Lagrangian coordinates by $\vec{\xi} = (\xi_1, \xi_3)$, then, Lagrangian coordinates follow the mean flow and satisfy

$$\frac{d\vec{\mathcal{X}}(\vec{\xi}, t)}{dt} = \vec{V}(\vec{\mathcal{X}}(\vec{\xi}, t), t). \tag{15}$$

Since the velocity fields that define Lagrangian coordinates in (15) are linear in space, the transformation map between Eulerian coordinates and mean Lagrangian coordinates can be expressed by a time-dependent matrix $M(t)$, with the incompressibility constraint, $\det M(t) = 1$:

$$\begin{aligned} \vec{\mathcal{X}}(\vec{\xi}, t) &= M(t)\vec{\xi} = \begin{pmatrix} M_{11}(t) & M_{12}(t) \\ M_{21}(t) & M_{22}(t) \end{pmatrix} \vec{\xi}, \\ \vec{\xi} &= M^{-1}(t)\vec{\mathcal{X}} = \begin{pmatrix} M_{22}(t) & -M_{12}(t) \\ -M_{21}(t) & M_{11}(t) \end{pmatrix} \vec{\mathcal{X}}. \end{aligned}$$

A simple calculation shows that the components of the transformation matrix satisfy the following equations:

$$\begin{aligned} \frac{dM_{11}}{dt} &= \frac{\bar{\omega}(t) + \sigma}{2} M_{21}(t), & \frac{dM_{21}}{dt} &= \frac{-\bar{\omega}(t) + \sigma}{2} M_{11}(t), \\ \frac{dM_{12}}{dt} &= \frac{\bar{\omega}(t) + \sigma}{2} M_{22}(t), & \frac{dM_{22}}{dt} &= \frac{-\bar{\omega}(t) + \sigma}{2} M_{12}(t). \end{aligned} \tag{16}$$

Since the Eulerian and Lagrangian coordinate frames coincide at time $t = 0$, the initial condition for $M(t)$ is the identity matrix,

$$M_{11}(0) = 1, \quad M_{12}(0) = 0, \quad M_{21}(0) = 0, \quad M_{22}(0) = 1.$$

The main benefit of the Eulerian-to-Lagrangian coordinate transformation is that the advective terms in (14) associated with the mean flow are absorbed into the transformation and disappear from the equations, while the nonlinear interaction of perturbations transforms invariantly. This change of variables yields the mean Lagrangian perturbation equations:

$$\begin{aligned} \omega_t + (\nabla_\xi^\perp \psi \cdot \nabla_\xi \omega) &= (M_{22}(t)\partial_{\xi_1} - M_{21}(t)\partial_{\xi_3})\rho, \\ \rho_t + (\nabla_\xi^\perp \psi \cdot \nabla_\xi \rho) + \frac{\partial \psi}{\partial \xi_1} &= 0, \\ L\psi &= \omega. \end{aligned} \tag{17}$$

Note that the Laplacian operator $\Delta = \partial_x^2 + \partial_z^2$ transforms into the linear operator L , which takes the following form in mean Lagrangian coordinates:

$$\begin{aligned} L &= (M_{12}(t)^2 + M_{22}(t)^2)\partial_{\xi_1 \xi_1}^2 + (M_{11}(t)^2 + M_{21}(t)^2)\partial_{\xi_3 \xi_3}^2 \\ &\quad - 2(M_{11}(t)M_{12}(t) + M_{21}(t)M_{22}(t))\partial_{\xi_1 \xi_3}^2. \end{aligned} \tag{18}$$

The equations in (17) and (18) allow simplifications for the special cases of mean flows discussed in Sec. II. For the readers' convenience we present the explicit simplified formulation for both purely vortical and shear flows in Appendix A.

Natural quantities that measure the intensity of evolving perturbations are the kinetic and potential energy defined as

$$\begin{aligned} E(t) &= KE(t) + PE(t), \\ KE(t) &= \frac{1}{2} \int \int |\vec{v}(\vec{\xi}, t)|^2 d\xi_1 d\xi_3, \\ PE(t) &= \frac{1}{2} \int \int \rho^2(\vec{\xi}, t) d\xi_1 d\xi_3. \end{aligned} \tag{19}$$

Here, \vec{v} and ρ are the perturbation Eulerian velocity and density fields. We point out that none of the energies above are conserved, as they can exchange energy with each other and also with the mean flow. Large portions of energy extracted from the mean flow may signify the onset of instability. In this paper we will consider perturbations with periodic structure in space, so that the integrations in the formulas in (19) above should be understood as integrals over the doubly periodic domain in Lagrangian coordinates.

Finally, we introduce the effective shear as an important measure that captures bulk effects of elementary flows over one time period. This notion will be extremely useful later in the paper when we discuss nonlinear stability of the elementary flows. By comparing the last two equations in (6) and the equations in (16) we observe that the density gradient components $b_1(t)$ and $b_3(t)$ coincide with the components $M_{21}(t)$ and $-M_{11}(t)$ of the coordinate transformation matrix. Since b_1 and b_3 are periodic functions of time, we conclude that $M_{11}(P)=1, M_{21}(P)=0$, where P is the period of $b_1(t)$ and $b_3(t)$; the incompressibility constraint $\det M(t) \equiv 1$ yields that $M_{22}(P)=1$. Thus, we conclude that $M(P)$ must have the following form:

$$M(P) = \begin{pmatrix} 1 & q \\ 0 & 1 \end{pmatrix} = e^{SP}, \tag{20}$$

where S is the 2×2 nilpotent matrix,

$$S = \begin{pmatrix} 0 & \gamma \\ 0 & 0 \end{pmatrix}. \tag{21}$$

The effective shear arises in a natural way in this context as the mean shear $\gamma = q/P$ over one period of the underlying elementary mean flow. In full agreement with this definition, purely vortical flows have zero effective shear, while for shear flows the effective shear is identical with the conventional shear.

D. The numerical method and diagnostics

The nonlinear stability of elementary flows in two space dimensions is studied in Secs. IV–VI. With the nonlinear equations for perturbations in mean Lagrangian coordinates from (17) and (18), we utilize a standard filtered pseudo-spectral method¹⁶ with fourth-order Runge–Kutta time differencing. Both for the physical interpretation of results as well as a numerical check on the accuracy of the time-stepping procedure, we monitor the kinetic and potential energy of perturbations from (19). All of the simulations reported below utilize $(128)^2$ Fourier modes and the initial data for perturbations is concentrated uniformly on the low wave number band $|k_1| + |k_3| \leq 10$ with random phases and total energy fluctuations representing 10% of the mean flow value.

Both to monitor the accuracy of the simulations with the given spatial resolution as well as to give physical insight into the nonlinear transfer of energy between scales, we monitored the energy in the six bands, $|k_1| + |k_3| \leq 10$, $10 < |k_1| + |k_3| \leq 20$, $20 < |k_1| + |k_3| \leq 30$, $30 < |k_1| + |k_3| \leq 40$, $40 < |k_1| + |k_3| \leq 50$, and $50 < |k_1| + |k_3| \leq 64$. In all the simulations reported in Secs. IV–VI, through this diagnostics, we

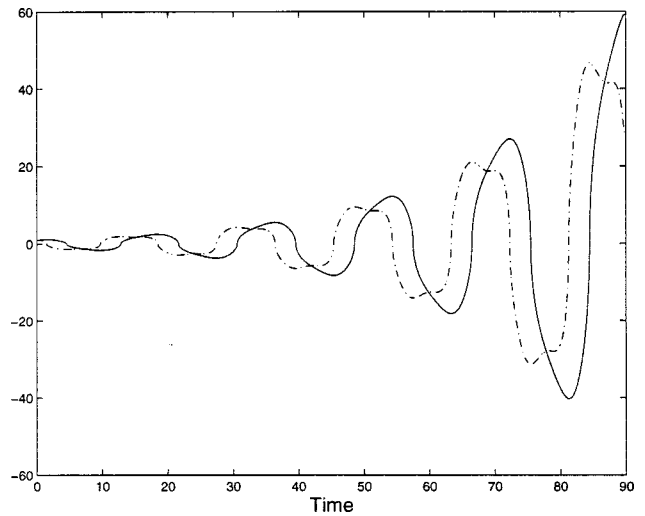


FIG. 1. Amplitudes of the perturbation vorticity (solid line) and perturbation density (broken line), represented by $\text{sgn}(\hat{\omega}_k(t))\sqrt{|\hat{\omega}_k(t)|}$ and $\text{sgn}(\hat{\rho}_k(t)) \times \sqrt{|\hat{\rho}_k(t)|}$, undergo exponential growth in time via parametric instability, for elementary vortical flow with $\mathcal{R}i=3$ and for wavelike perturbations aligned along the direction of maximum growth, $\alpha_0 \approx 2.75$.

concluded that the energy of perturbations remained confined essentially to wave numbers, $0 < |k_1| + |k_3| \leq 30$, so that the spatial resolution of $(128)^2$ Fourier modes is completely justified.

III. LINEAR STABILITY THEORY

In this section we will set up the linear stability analysis of the elementary exact solutions in (5)–(7). The results of this section, interesting on their own, will serve as a basis for the fully nonlinear stability studies which we will describe in Secs. (IV)–(VI).

Linear stability analysis for the elementary exact flows is based on an exact solution procedure described in detail elsewhere,^{12,14} but here we use a simpler Lagrangian formulation. In brief, we consider wavelike perturbations to the elementary exact solutions in (5)–(7), in the mean Lagrangian coordinates and with a fixed wave number. The shape of the wavefronts and the numerical values of the spatial period are irrelevant for stability considerations; for convenience we select waves with a sinusoidal shape of period 2π in both spatial directions:

$$\psi(\vec{\xi}, t) = \hat{\psi}_k(t) \sin(\vec{k} \cdot \vec{\xi} + \phi_0) = \hat{L}_k^{-1} \hat{\omega}_k(t) \sin(\vec{k} \cdot \vec{\xi} + \phi_0), \tag{22}$$

$$\omega(\vec{\xi}, t) = \hat{\omega}_k(t) \sin(\vec{k} \cdot \vec{\xi} + \phi_0), \quad \rho(\vec{\xi}, t) = \hat{\rho}_k(t) \cos(\vec{k} \cdot \vec{\xi} + \phi_0).$$

Here, \vec{k} is a fixed wave vector with integer coordinates and ϕ_0 is an arbitrary phase shift. An easy check shows that the wavelike perturbations in (22) satisfy the equations in (17); in addition, it is easy to show that all the nonlinear cross-gradient terms vanish completely, so that the equations in (17) assume the following linear form:

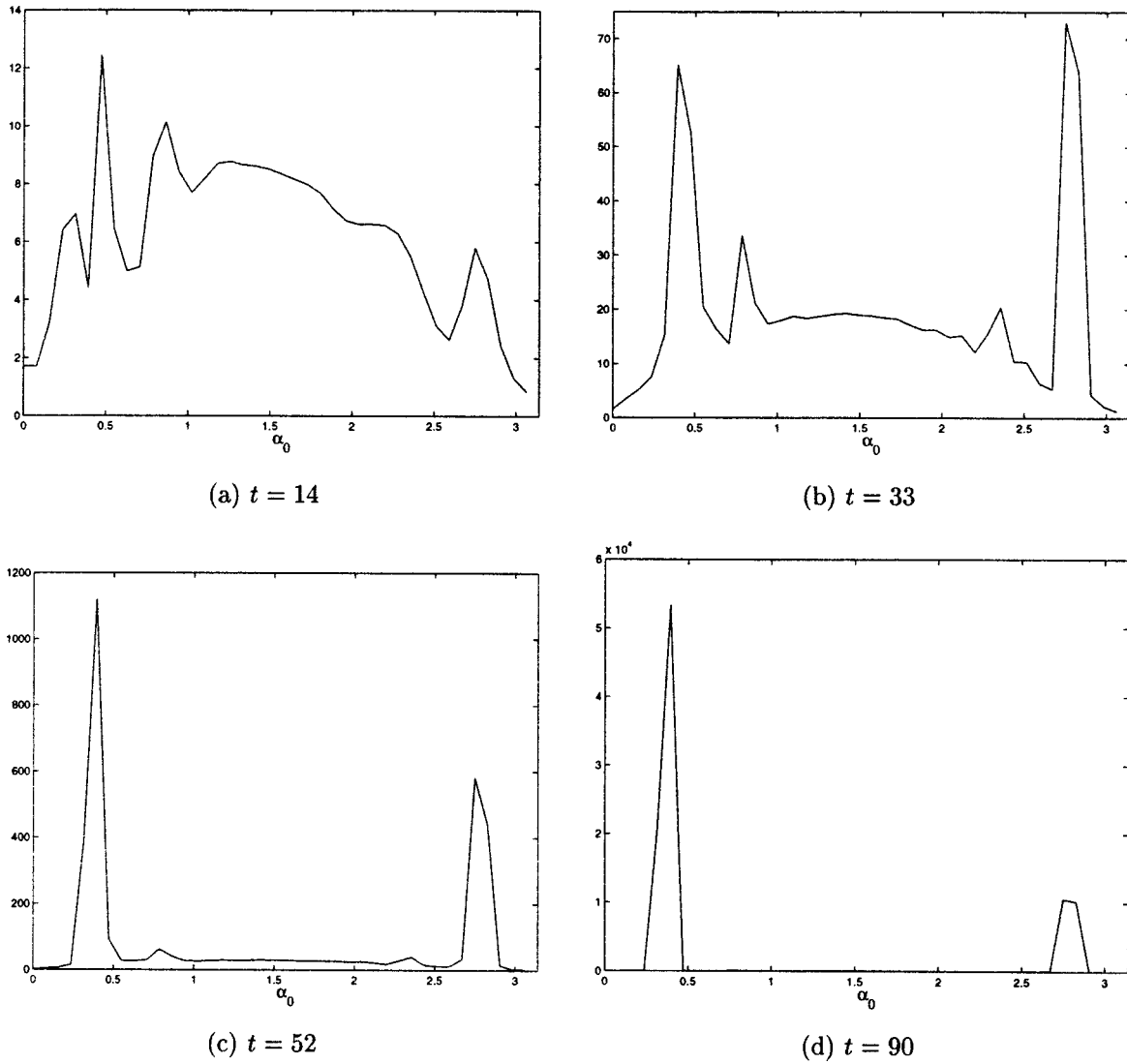


FIG. 2. Total perturbation energy, $E(t)$, as function of wave inclination angle, α_0 , maximized over all initial conditions of unit strength, at four different moments of time for vortical flow with $\mathcal{R}i=3$.

$$\frac{d\hat{\omega}_k}{dt} = -(M_{22}(t)k_1 - M_{21}(t)k_3)\hat{\rho}_k(t), \tag{23}$$

$$\frac{d\hat{\rho}_k}{dt} = -k_1\hat{L}_k^{-1}\hat{\omega}_k,$$

where \hat{L}_k is the linear time-dependent spatial operator, that originates from the two-dimensional Laplacian in Eulerian coordinates, and \hat{L}_k^{-1} is its inverse,

$$\hat{L}_k = -[(M_{12}(t)^2 + M_{22}(t)^2)k_1^2 + (M_{11}(t)^2 + M_{21}(t)^2)k_3^2 - 2(M_{11}(t)M_{12}(t) + M_{21}(t)M_{22}(t))k_1k_3], \tag{24}$$

$$\hat{L}_k^{-1} = -[(M_{12}(t)^2 + M_{22}(t)^2)k_1^2 + (M_{11}(t)^2 + M_{21}(t)^2)k_3^2 - 2(M_{11}(t)M_{12}(t) + M_{21}(t)M_{22}(t))k_1k_3]^{-1}.$$

One can obtain a more specific form of (14) for the two special cases of elementary mean flows we considered in Sec. II B, i.e., purely vortical and shear flows. The system in (23) for the vortical flows reduces to

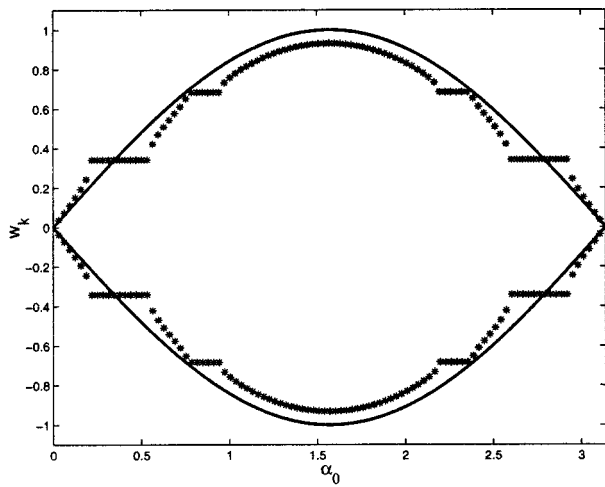
$$\frac{d\hat{\omega}_k}{dt} = -[\cos \theta(t)k_1 - \sin \theta(t)k_3]\hat{\rho}_k, \tag{25}$$

$$\frac{d\hat{\rho}_k}{dt} = \frac{k_1}{|\vec{k}|^2}\hat{\omega}_k,$$

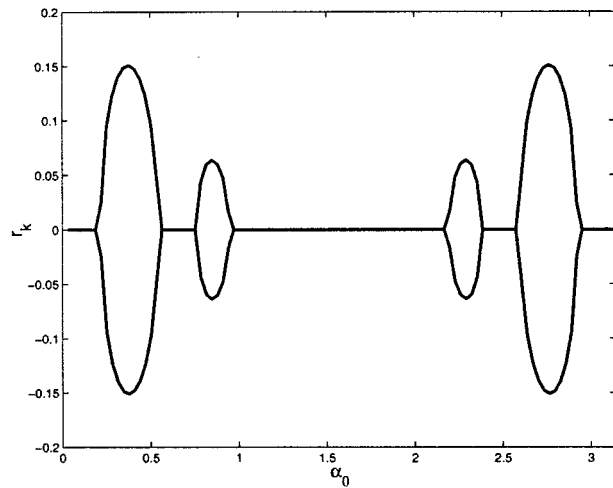
and is equivalent to Hill's equation:

$$\frac{d^2}{dt^2}\hat{\rho}_k = -P(t)\hat{\rho}_k(t),$$

$$P(t) = \frac{k_1}{|\vec{k}|^2}[k_1 \cos \theta(t) - k_3 \sin \theta(t)].$$



(a) Phase



(b) Growth Rate

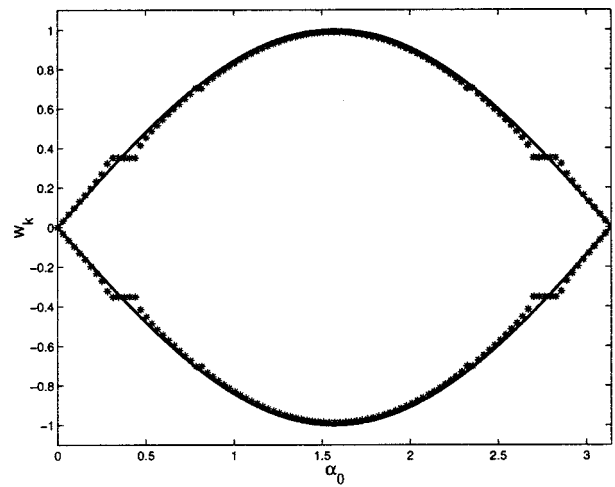
FIG. 3. Phase (a) and growth rate (b) for wavelike perturbations as function of the wave inclination angle, α_0 , for Richardson number, $Ri=1$, with conventional Richardson number 16 times the critical value of $1/4$. Thin solid lines depict dispersion curves for inertial gravity waves on the phase diagram (a).

where $\theta(t)$ solves the pendulum equation in (11) and (12). For shear flows Eq. (23) has the form

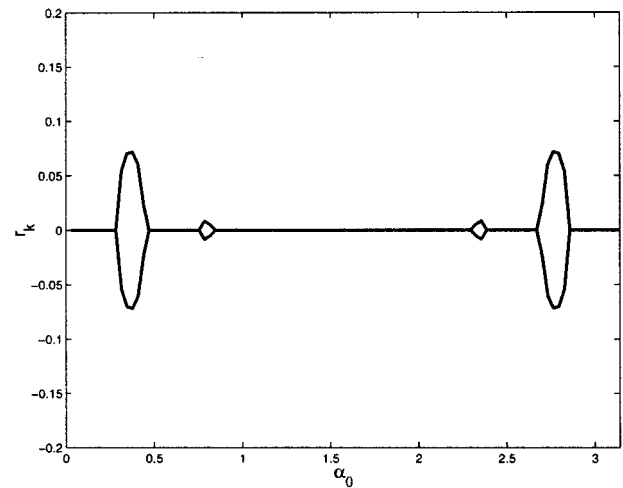
$$\frac{d\hat{\omega}_k}{dt} = -k_1 \hat{\rho}_k(t), \quad \frac{d\hat{\rho}_k}{dt} = -k_1 \hat{\psi}_k(t), \tag{26}$$

$$-((\bar{\omega}_0^2 t^2 + 1)k_1^2 + k_3^2 - 2\bar{\omega}_0 t k_1 k_3) \hat{\psi}_k(t) = \hat{\omega}_k(t).$$

As we have shown above, the linear stability analysis of elementary flows is reduced to studying a simple 2×2 linear system with time-dependent coefficients for each spatial wave number. We note that as regards to two-dimensional flows, the equations in (23) are entirely equivalent to the more complicated system utilized for stability analysis developed earlier for general three-dimensional perturbations in the Eulerian frame.¹² The detailed proof of this statement can be found in Appendix B.



(a) Phase



(b) Growth Rate

FIG. 4. As for Fig. 3, with Richardson number, $Ri=5$, with conventional Richardson number 80 times the critical value of $1/4$.

Next, we briefly describe the stability analysis for the system in (23), which was performed via direct numerical computation for various mean flows. For purely vortical flows it is possible to apply simple Floquet theory to study (23) in a very precise way;¹² for flows of general form, unfortunately, one cannot benefit from this approach, since the coefficients in (23) are not periodic functions of time. We also point out here that predictions of the linear theory should be treated with caution, since nonlinear interaction mechanisms start playing a dominant role as amplitudes grow larger. From this perspective, we will be more interested in studying transient behavior of solutions to (23) as a potential mechanism for nonlinear interactions, than in the ultimate stability of these solutions. In our simulations for linear stability, we investigated transient growth of perturbations for various elementary flows, generated by solutions to (23) at several specified times. We utilized a numerical procedure which we will describe next.

For each elementary flow the list of parameters involved

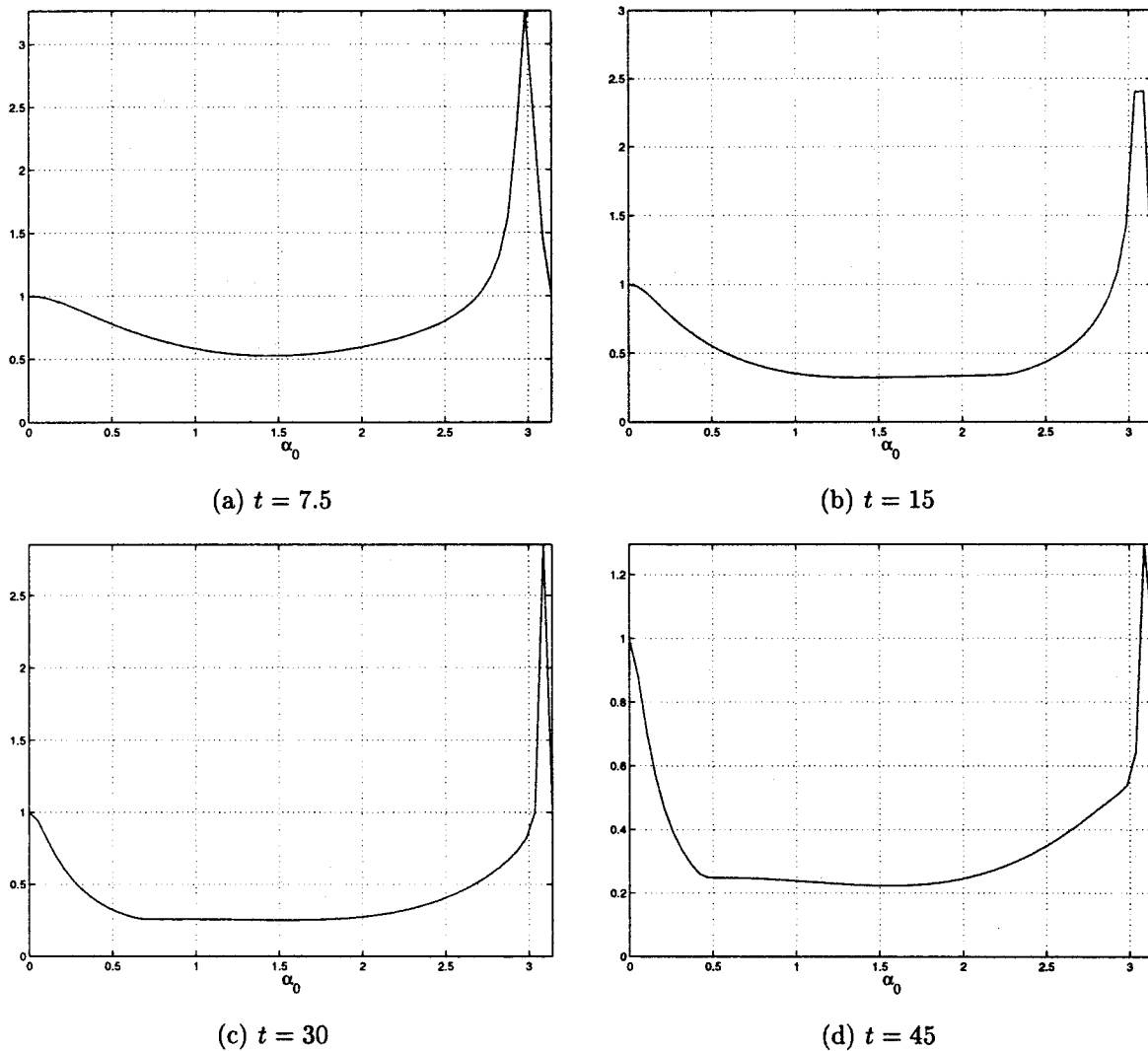


FIG. 5. Total perturbation energy, $E(t)$, as function of wave inclination angle, α_0 , maximized over all initial conditions of unit strength, at four different moments of time for shear flow with $\mathcal{R}i=1$.

in the linear stability analysis includes: (a) the inclination angle of a wave, α_0 , where $k_1 = \sin \alpha_0$, $k_3 = -\cos \alpha_0$; (b) the initial values of perturbation amplitudes, expressed in polar coordinates, $\hat{\omega}_k(0) = R \sin \beta$; $\hat{\rho}_k(0) = R \cos \beta$. We remark that in the linear theory the strength of initial perturbations R plays no role; therefore, we can reduce the parameter set to the two angles, α_0 and β . Next, for each wave inclination angle, α_0 , we maximized the value of total perturbation energy $E(t)$ defined in (19) over all initial conditions, parametrized by the angle β . The transient growth diagrams, which will be presented later in this section, show the maximum value of energy E as function of the inclination angle α_0 . In the three subsections below we address the results of linear stability analysis separately for purely vortical flows, shears, and elementary flows of general form.

A. Pendulum flows

Some of the linear stability analysis results for purely vortical flows were reported by the authors in an earlier paper,¹² where we showed through detailed Floquet analysis

that for all Richardson numbers vortical flows are linearly unstable. Instability develops most rapidly for plane waves directed along certain preferred directions, with bands of weaker instability surrounding these directions. The instability observed in the linear theory is of parametric type and results in exponentially growing oscillations whose period is twice the period of the underlying ‘‘pendulum’’ flow in (A1) and (A2). A typical picture of parametric instability that arises in this case is given in Fig. 1 for the vortical flow with $\mathcal{R}i=3$. To emphasize the structure of the instability, we display the evolution of these perturbations for 10 periods of the mean flow. Instead of perturbation amplitudes themselves, we plot quantities $\text{sgn}(\hat{\omega}_k(t))\sqrt{|\hat{\omega}_k(t)|}$ and $\text{sgn}(\hat{\rho}_k(t))\sqrt{|\hat{\rho}_k(t)|}$ for better visualization, so that the five growing oscillations of parametric instability are clearly recognizable. Despite the fact that dependence of stability properties on the inclination angle α_0 can be found in a direct fashion via Floquet theory, we choose to include Fig. 2, which shows transient amplification of the perturbation energy $E(t)$ defined in (19), sampled at times $t = 14, 33, 52$ and 90 , and normalized so that $E(0) = 1$. This plot reinforces the point that transient ampli-

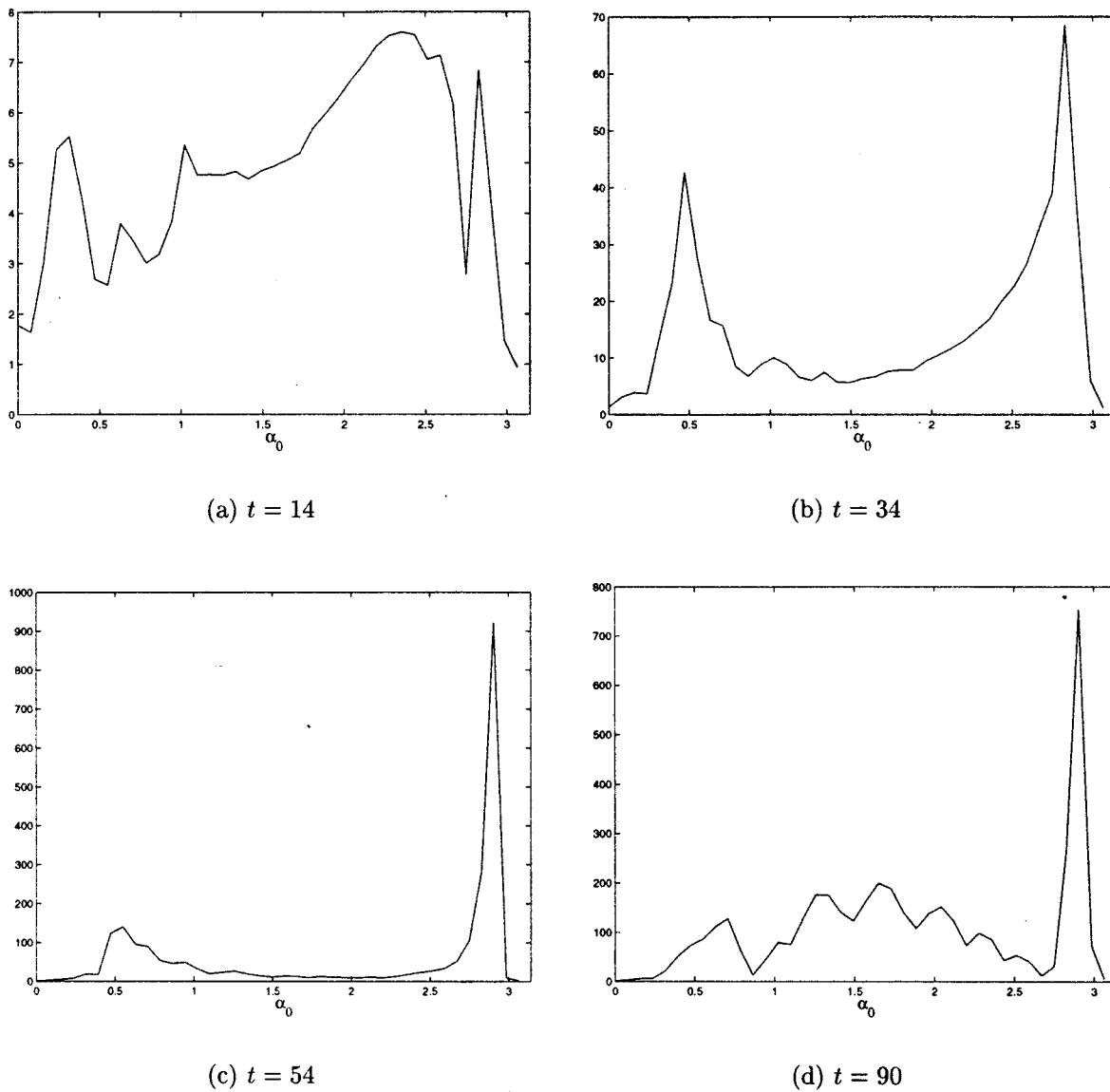


FIG. 6. Transient growth of perturbation energy, $E(t)$, as function of wave inclination angle, α_0 , maximized over all initial conditions of unit strength, depicted at four different moments of time for flow with $Re=3$ and effective shear $\gamma=0.05$.

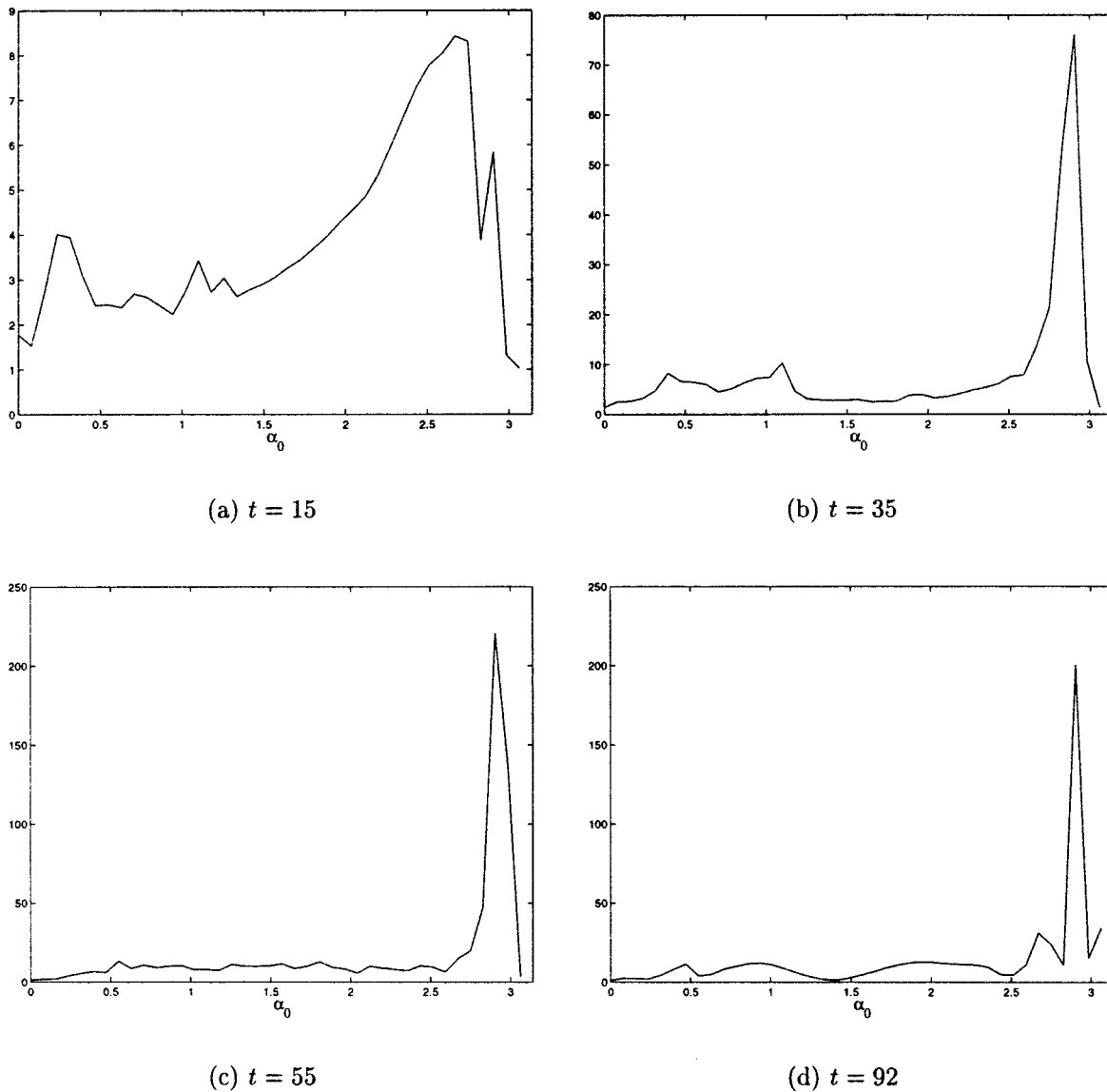
fication is more valuable for our study than precise instability. The organization along the preferred directions and surrounding areas of instability is clearly visible at all times, but becomes more apparent at later moments.

An important question related to the plane waves involved in this study is the following: How different are these waves from regular gravity waves? We will address this question next by constructing and comparing the dispersion curves for both classes of waves. For each wave number $\vec{k} = (k_1, k_3)$ we consider the eigenvalues and eigenvectors¹² arising in Floquet theory for (25). For the initial data $\hat{\rho}_k(0)$, $\hat{\omega}_k(0)$ taken along an eigenvector \vec{e} , we obtain the following representation of the perturbation amplitude vector at the period time P :

$$\begin{pmatrix} \hat{\rho}_k(P) \\ \hat{\omega}_k(P) \end{pmatrix} = \exp(-i w_k P) \exp(r_k P) \vec{e}. \quad (27)$$

Here, \vec{k} is related to the wave inclination angle α_0 via

$(k_1, k_3) = |\vec{k}|(\sin \alpha_0, -\cos \alpha_0)$, and $(r_k - i w_k)$ is the logarithm of the Floquet multiplier normalized by P which corresponds to the eigenvector \vec{e} ; as usual, we select waves of sinusoidal shape for convenience. Since the Floquet matrix is purely real and has trace zero for all vortical flows,¹² its eigenvalues are either two real numbers with equal magnitudes and of opposite sign, or two purely imaginary and conjugate numbers. As a result, we conclude that either $w_k = 0, r_k \neq 0$ or $w_k \neq 0, r_k = 0$ must hold for the expression in (27). In Figs. 3 and 4 we present the dispersion curves for vortical flows at $Re=1$ and $Re=5$. The phases w_k are plotted against the wave vector \vec{k} parametrized by the inclination angle α_0 in Figs. 3(a) and 4(a). Complementary plots of growth rates r_k as function of α_0 are shown in Figs. 3(b) and 4(b). Note that the flat regions in the growth rate diagrams correspond to stability and nontrivial dependence for the phases, while the flat regions in the phase diagrams corre-

FIG. 7. As for Fig. 6, for flow with $\mathcal{R}i=3$ and effective shear $\gamma=0.1$.

spond to instability.

In the context of our formulation, gravity waves correspond to the wave-like perturbations of constant density gradient field, with the dispersion relation given by

$$w = \pm \sin \alpha_0.$$

Obviously, gravity waves in a static medium have no growth, therefore $r_k \equiv 0$ for them. To illustrate the differences between the two types of waves we added dispersion curves for gravity waves to Figs. 3(a) and 4(a). Flat regions on these diagrams correspond to instability and vividly distinguish the two dispersion relations. The discrepancies in the dispersion curves in the bands of stability, $r_k=0$, are clearly visible in all of the plots, especially for $\mathcal{R}i=1$, with typical phase speeds of perturbations waves 10% smaller than typical phase speeds of gravity waves. Recall that $\mathcal{R}i=1$ corresponds to a value of Richardson number, 16 times larger than the classical value for shear instability, $Ri=1/4$. Note that

these discrepancies eventually become less pronounced for the larger values of $\mathcal{R}i$, as in Fig. 4 and disappear as $\mathcal{R}i \rightarrow +\infty$.

B. Shear flows

Vertical shear flows are the traditional testing ground for stability studies. Miles and Howard established the threshold of $1/4$ for linear stability and instability exactly for this type of flow.^{5,6} General linear stability of shear flows at high Richardson numbers in the framework of elementary exact solutions in (5)–(7) was confirmed earlier,¹² with the following comment. At short times perturbations to shear flows exhibit transient non-normal growth that does not lead to the development of instability in a formal sense. Still, this non-normal transient behavior may play a role in the build up of the nonlinear mechanisms of instability. This issue will be studied in more detail in Sec. V. In addition to the bands of non-normal behavior in a number of shear flows we studied, there exists a marginally stable mode, characterized by the

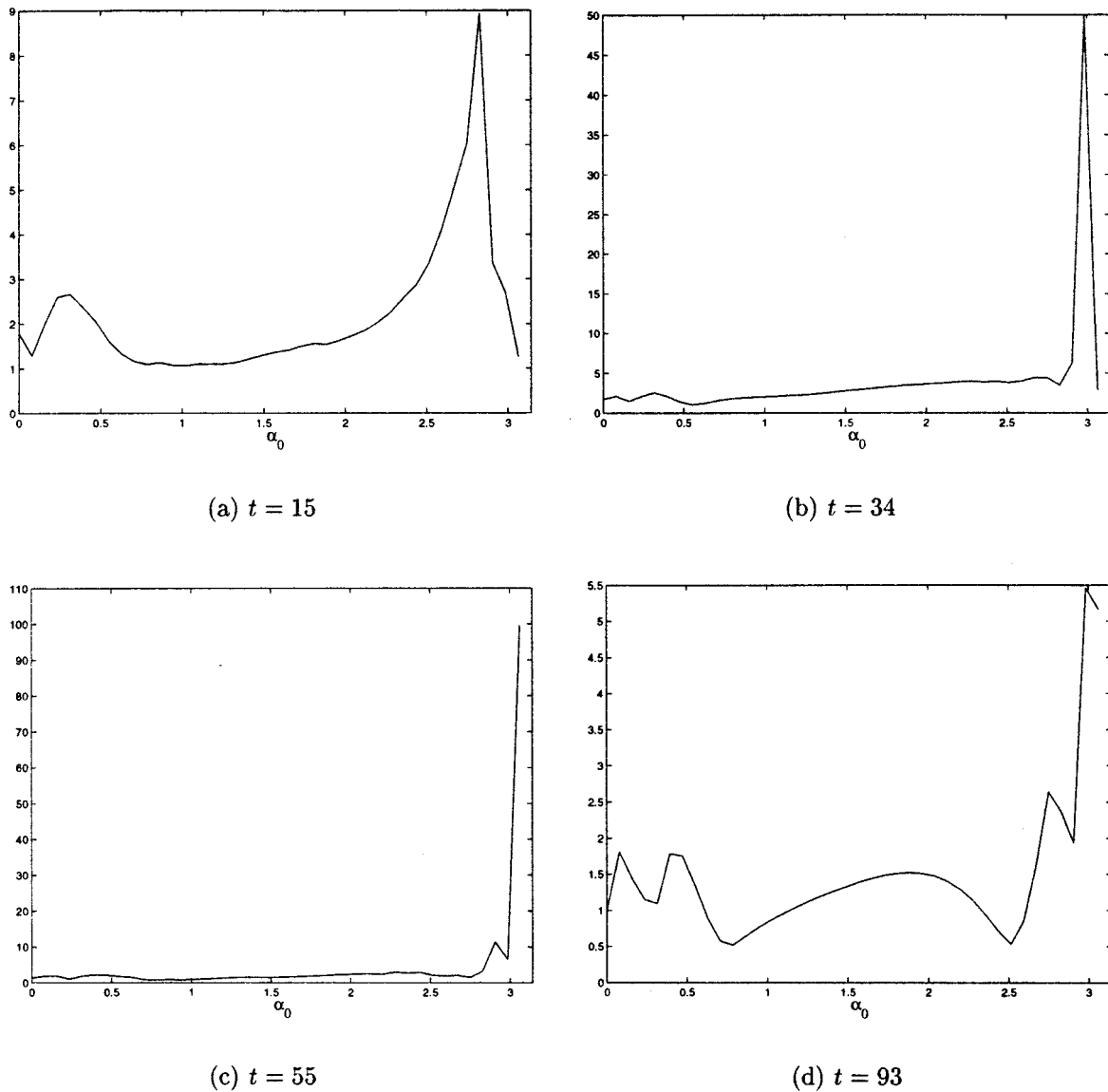


FIG. 8. As for Fig. 6, for flow with $\mathcal{R}i=3$ and effective shear $\gamma=0.22$.

linear growth of perturbation amplitudes.^{17,12}

To illustrate how perturbations undergo transient growth, in Fig. 5 we present plots of perturbation energy $E(t)$ for various wave inclinations α_0 , maximized over all initial conditions and normalized so that $E(0)=1$. We selected four different moments of time, $t=7.5, 15, 30$, and 45 to illuminate the motion of the maximum energy spike towards the position of the marginally stable mode at $\alpha_0=\pi$. We remark that the position of the spike in each of these plots recovers the direction of optimal perturbation for non-normal flows.¹⁸

C. Transient mixed flows

Wavelike perturbations to purely vortical flows are described by the linear system in (17), whose coefficients are periodic functions of time. In the general case, the coefficients of the coordinate transformation $M(t)$ are not periodic, so that one cannot utilize the convenient technique of Floquet theory. Since in this work we view linear stability

analysis mainly as a tool to obtain maximum transient amplification and to predict optimal perturbations for the non-linear stability studies, we will restrict our goal to finding wave inclination angles that correspond to the fastest transient growth at various specified times.

As an illustrative example, we report three typical examples of transient behavior for elementary flows with features of both vortical and shear flows in Figs. 6–8. These figures correspond to elementary mean flows with $\mathcal{R}i=3$ and effective shear $\gamma=0.05, 0.1$, and 0.22 , as defined at the end of Sec. II C. In each plot we present the distribution of transient energy amplification ratio, $E(t^*)/E(0)$, as a function of the wave inclination angle α_0 , maximized over a wide range of initial conditions in a fashion described in the first part of Sec. III. Here t^* is an arbitrary moment of time, selected to represent transient behavior, and $E(t)$ is the total perturbation energy defined in (19). We observe that at short times the flows with small effective shear (compare Fig. 7 with Fig. 2) behave similarly to purely vortical flows. The

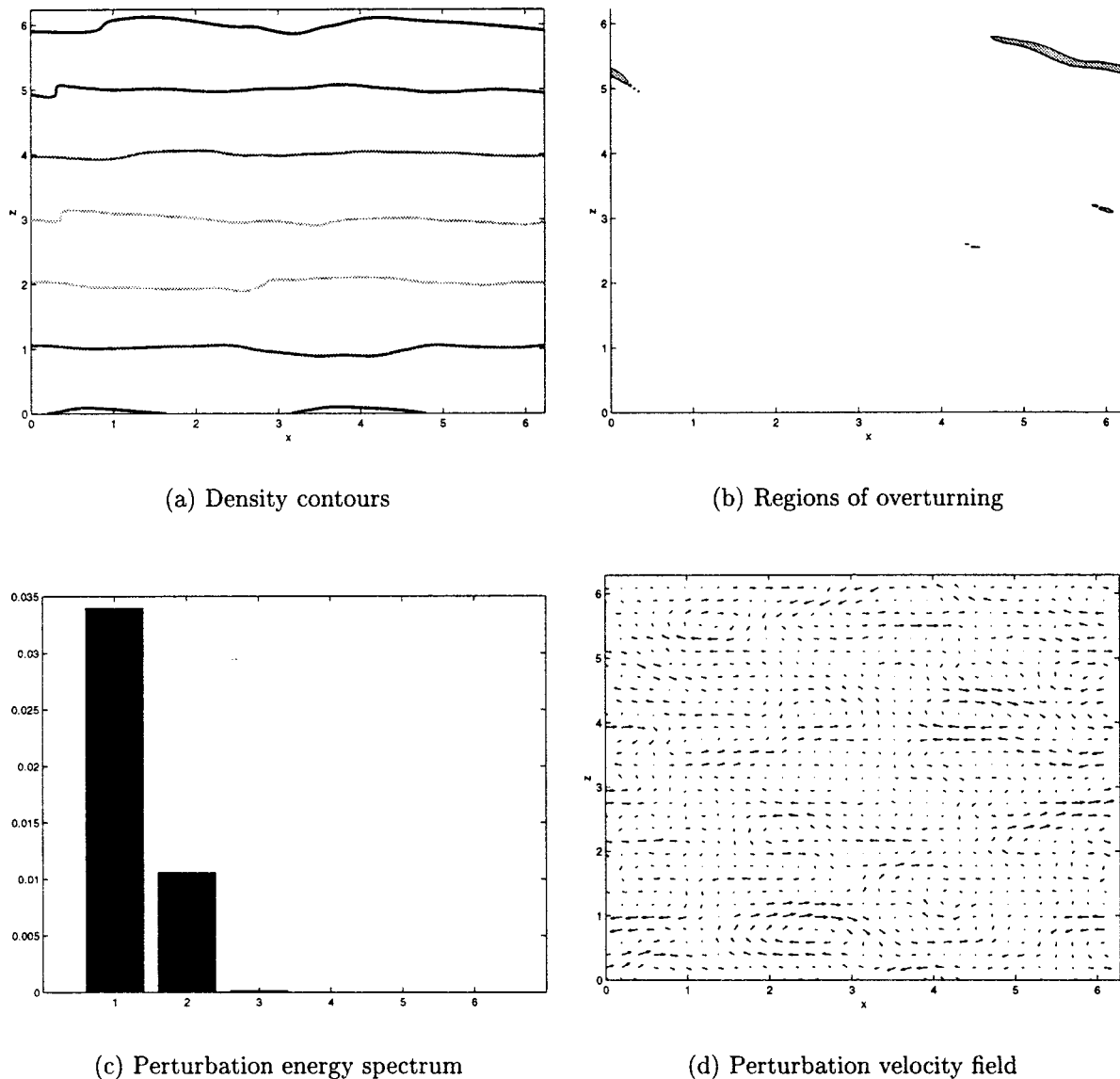


FIG. 9. Density contours, regions of local overturning, spectral distribution of energy and velocity field of perturbation to the vortical flow with $Ri=3$, at $t=36$. Heights of the six bars in the energy distribution plot indicate the amount of energy allocated in Fourier modes with wave numbers, $|k_1|+|k_3| \leq 10$, $10 < |k_1|+|k_3| \leq 20$, $20 < |k_1|+|k_3| \leq 30$, $30 < |k_1|+|k_3| \leq 40$, $40 < |k_1|+|k_3| \leq 50$, $50 < |k_1|+|k_3| \leq 64$.

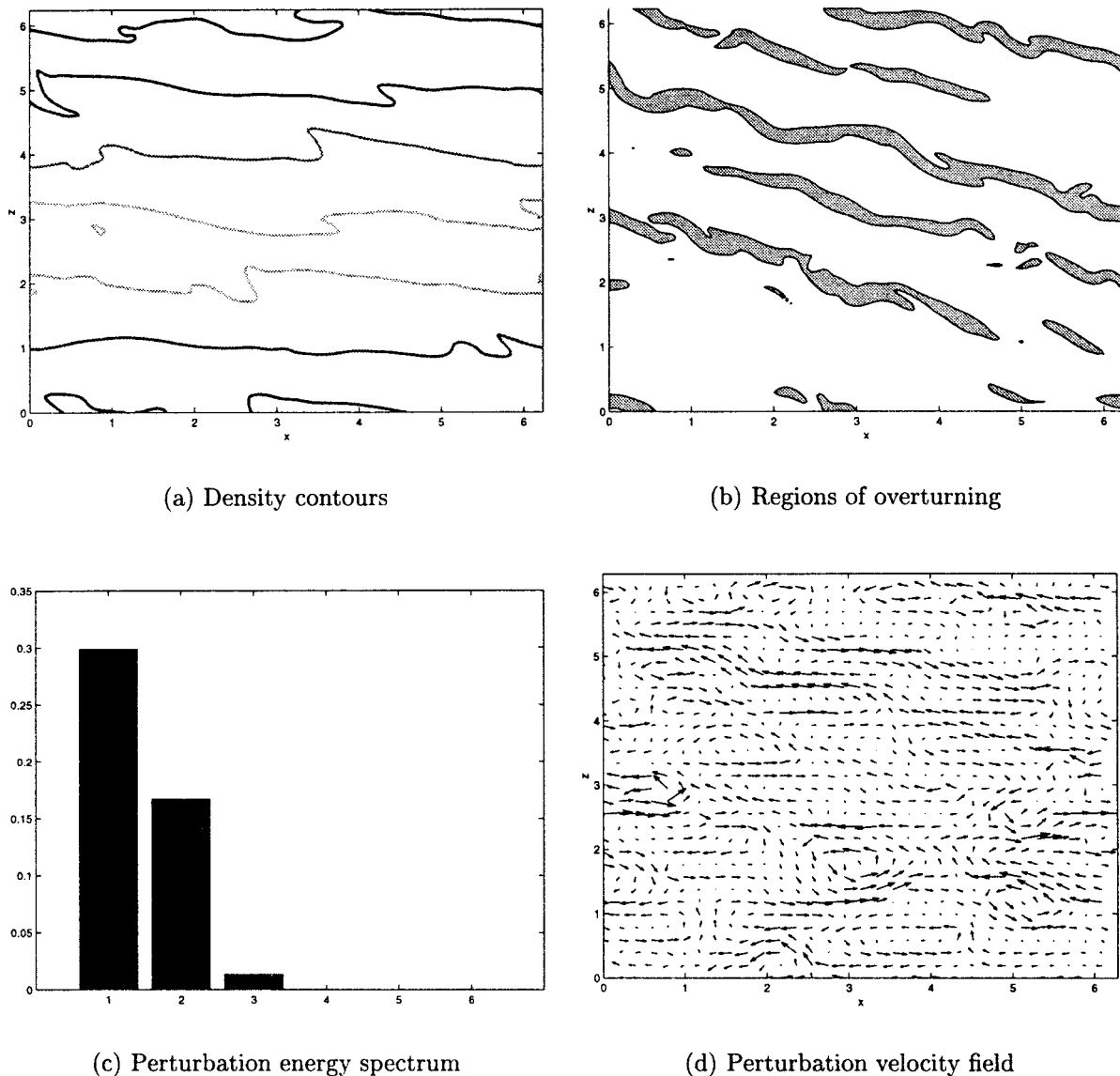
two peaks of fastest growth in Fig. 2, and the bands of instability surrounding them are clearly visible in Figs. 6(a), 6(b), 7(a), 7(b), and 8(a). Such vortical-like behavior does not persist at longer times, as shown in Figs. 6(c), 6(d), 7(c), 7(d), and 8(c), 8(d) where the modes of amplification are distributed more like those of a shear, as evident from comparison with Fig. 5.

IV. PENDULUM FLOWS AND OVERTURNING

To investigate whether perturbations to vortical flows, given by (A1), grow in time in the fully nonlinear regime we integrate the equations in (17) with a standard pseudo-spectral method¹⁶ on a rectangular grid with a resolution of $(128)^2$ Fourier modes. We chose random large-scale initial data by assigning random amplitudes and random phases to Fourier modes with wave numbers restricted by $|k_1|+|k_3| \leq 10$. The values of the random amplitudes were selected in

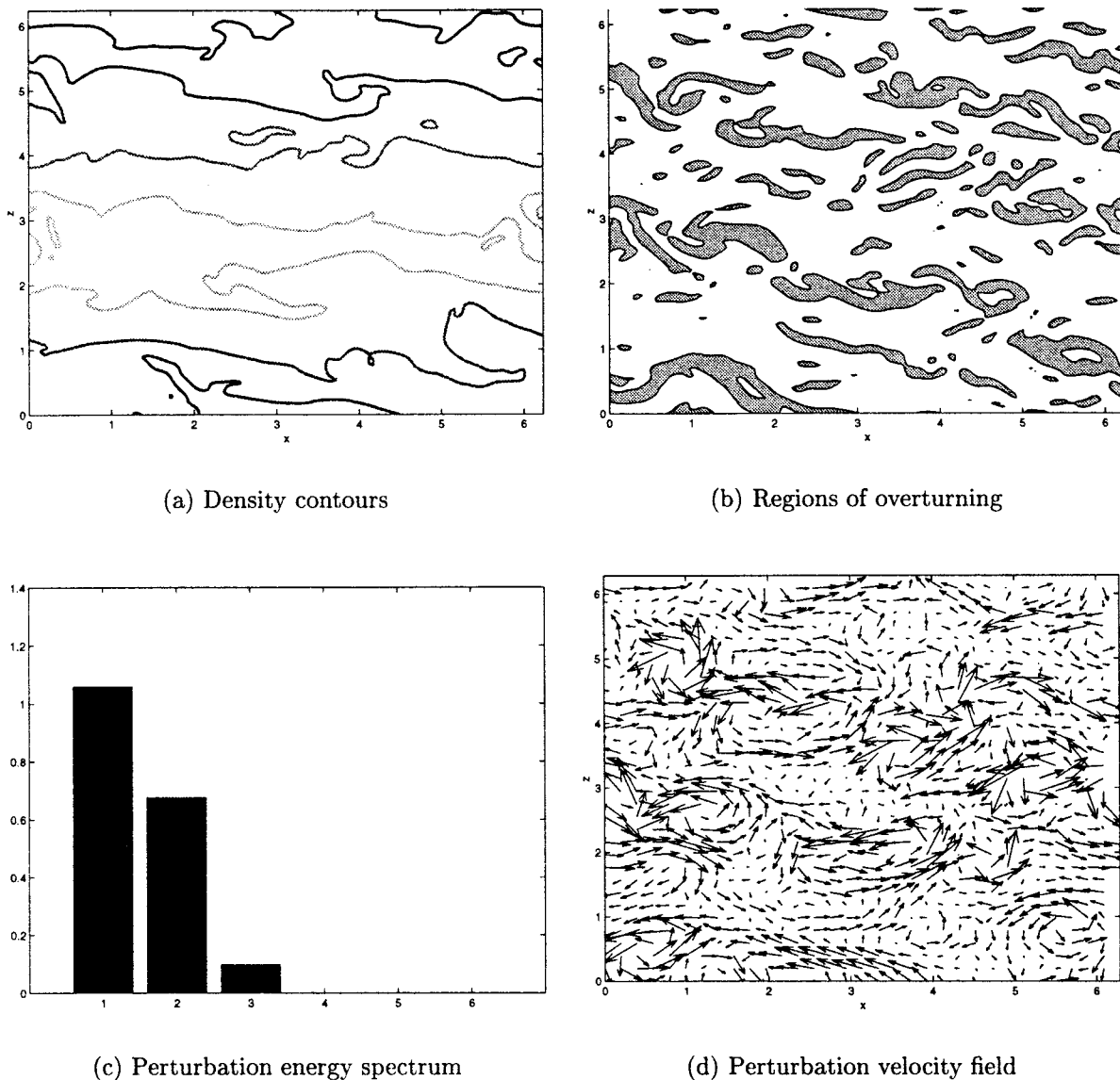
such a way that the initial energy fluctuations are 10% of the mean flow energy. The main results will be summarized in this section for $Ri=3$.

We illustrate the development of perturbations with plots of perturbation energy and some snapshots of representative density contours, velocity field, spectral energy distribution and the regions of overturning. Local overturning takes place when the total density gradient satisfies $d\bar{p}/dz > 0$. It is convenient to take the snapshots at the whole periods of the mean vortical flow in (A1), when the Eulerian and Lagrangian coordinate systems coincide exactly. As an illustrative example we selected a vortical mean flow with $Ri=3$, with the period roughly equal to 9 buoyancy times. We note, as a side remark, that value 3 of the Richardson number corresponds to $Ri=12$ when the conventional definition of Richardson number is used, and, thus, is 48 times greater than the critical value given by the Miles–Howard theorem. Figures 9–11 show flow parameters after 4, 6, and 8 periods of the

FIG. 10. As for Fig. 9, at $t=54$.

mean flow. The slight perturbations at 4 periods shown in Fig. 9, present only very limited overturning, depicted by shaded regions in Fig. 9(b), and are strongly aligned along the direction with the inclination angle, $\alpha_0 \approx 2.75$. This direction is easily identifiable with the direction of fastest growth predicted by the linear theory and shown in Fig. 2. Note that at this stage most of the perturbation energy is concentrated in large scales, as shown in Fig. 9(c). At the later times, presented in Figs. 10 and 11, the perturbations cause violent overturning throughout the domain of integration. The velocity field in Fig. 10(d) and overturning regions in Fig. 10(b) are still largely organized along the preferred direction predicted by the linear theory. The regions of strong shear are visible in Fig. 10(d). According to conventional expectations, they become subject to shear instability, whose typical signature is obvious in Fig. 11. The overturning regions shown in Fig. 11(b) overtake the whole integration domain, with well-formed intensive structures resembling Kelvin–Helmholtz billows.¹⁹ The coherent same-sign vortices corresponding to the overturning regions appear in

Fig. 11(d). We point out that the spectrum of perturbation energy undergoes considerable spreading, with substantial amounts transferring to the smaller scales, as seen in Figs. 9(c), 10(c), 11(c). Plots of the potential and kinetic energy budgets of the perturbation, shown in Fig. 12, give a very revealing picture of the instability development. At early stages, when perturbation amplitudes are relatively small, parametric instability of the linear theory, shown in Fig. 1, is clearly the main driving mechanism of amplification. Near $t=80$ nonlinear interactions start dominating the flow and change the picture completely. The time of transition to the nonlinear regime of instability development correlates very well with the emergence of the direct cascade to small scales in the spectrum and formation of the Kelvin–Helmholtz-type billows shown in Figs. 9(c), 10(c) and 11(c). Although the energy spectrum spreads over three bands with $|k_1| + |k_3| \leq 30$, we note that our numerical procedure produces reliable answers, since the bands of the spectrum with $64 \geq |k_1| + |k_3| > 30$ remain very weakly excited. Qualitatively similar results were observed in numerical experiments with vortical

FIG. 11. As for Fig. 9, at $t=72$.

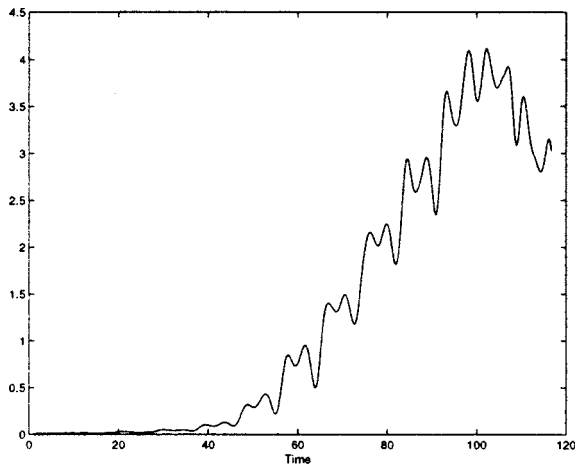
flows at $Ri=1,5,10$, which are not reported in this paper. A preliminary study with $Ri=5$ has been reported elsewhere.²⁰ As one may naturally expect, instabilities take a longer time to develop as the Richardson numbers grow, but strong overturning with nonlinear saturation and structures resembling Kelvin–Helmholtz instability were observed at all Richardson numbers we studied.

V. SHEAR FLOWS

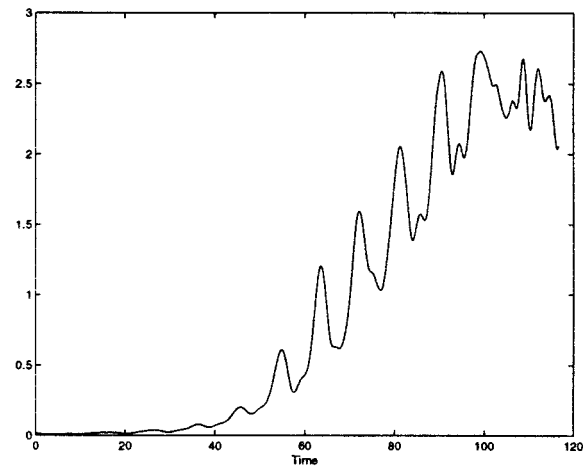
We investigated the stability properties of elementary shear flows, given by (26), utilizing the pseudo-spectral code in mean Lagrangian coordinates. The preliminary runs with random large scale initial conditions, such as described in Sec. IV, revealed no significant amplification in the perturbation amplitudes for all flows tested, with $Ri=1,3,5$. The results we report here were produced by integrating the equations in (A4) with the initial conditions of the following form. We selected the plane wave, whose direction provides the fastest transient growth within the linear theory, de-

scribed in Sec. III C, and added a random large-scale perturbation to this wave in order to include the nonlinear interactions in (17). The amplitudes of initial conditions were selected in such a way that the initial energy of fluctuations totaled 10%, with 90% of that energy assigned to the preferred wave, and the remaining 10% distributed uniformly with random phase among the other large scale modes. For this paper, we deliberately chose a flow with the smallest value of the Richardson number, $Ri=1$, to illuminate the robustness of stability demonstrated by this study. Other investigated shear flows ($Ri=3,5$) presented similar qualitative and quantitative features and are mentioned only briefly in this paper. Note that the conventionally defined Richardson numbers are 1.5 times greater than the values reported here.

The evolution of perturbations is illustrated by the characteristic density contours, velocity field, and the spectral distribution of perturbation energy plotted at the initial moment and at $t=4.5$, $t=9$, and $t=18$ buoyancy times, shown in Figs. 13–16. The density contours shown in Figs. 13(a),



(a) Kinetic energy

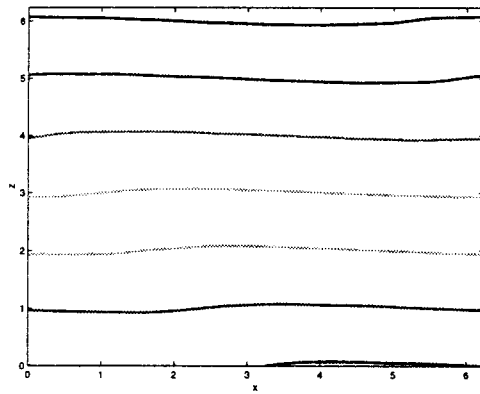


(b) Potential energy

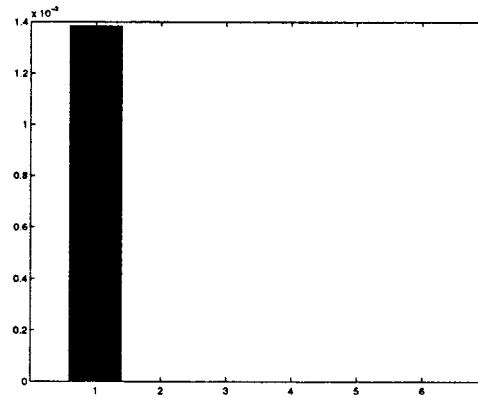
FIG. 12. Kinetic and potential energy of perturbation for vortical flow with $\mathcal{R}i = 3$.

14(a), 15(a), and 16(a), are plotted in the Eulerian frame, to emphasize that no overturning takes place for this flow. The Eulerian components of the velocity field shown in Figs. 13(c), 14(c), 15(c), 16(c) are stripped from the mean shear

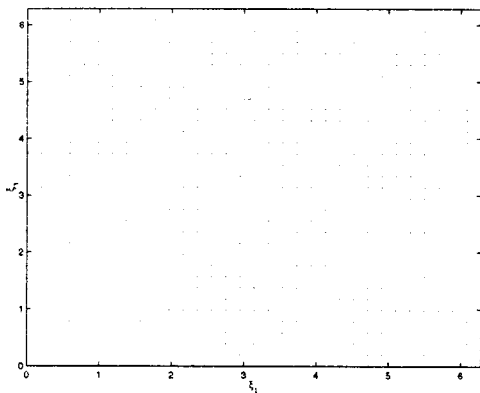
piece and are mapped back into the Lagrangian frame to show the detailed structure of the perturbation field. A general picture of perturbation evolution is given by the plots of potential and kinetic energy in Fig. 17. At an early time, t



(a) Density contours

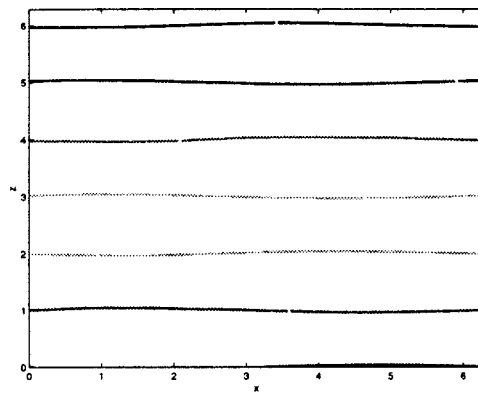


(b) Perturbation energy spectrum

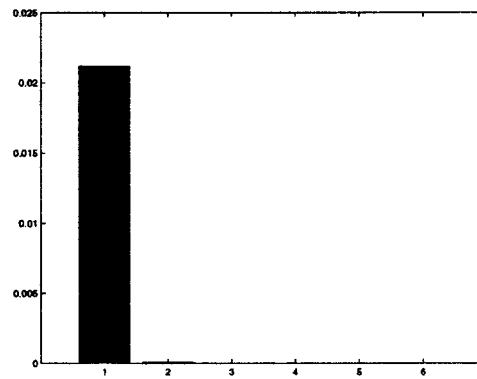


(c) Perturbation velocity field

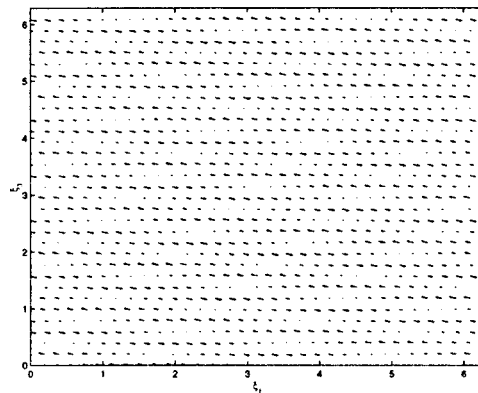
FIG. 13. Density contours, spectral distribution of energy and velocity field of perturbation to the shear flow with $\mathcal{R}i = 1$, at initial time $t = 0$. Bars in the plot of spectral distribution of energy are as in Fig. 9.



(a) Density contours



(b) Perturbation energy spectrum



(c) Perturbation velocity field

FIG. 14. As in Fig. 13, at $t=4.5$.

$=4.5$, presented in Fig. 14, the perturbation velocity field is growing and is visibly organized along the preferred direction. At this time, the density contours are only slightly deflected from their unperturbed horizontal locations. At a later time, $t=9$, the density contours are visibly deflected [see Fig. 15(a)]. Due to the strong shearing effect of the mean flow, however, no overturning is produced. The velocity field shown in Fig. 15(c) at the same moment is strongly amplified and has the structure of a quasitraveling gravity wave going through the domain rather than a shear; the arrows reflecting streamlines are directed towards the wave fronts rather than along them. Note that the angle of inclination of the wave fronts coincides accurately with the optimal perturbation direction, $\alpha^* \approx 3$, shown in Fig. 5. In Fig. 16 we observe the complete decay of the perturbations occurring at $t=18$. We remark on the spectral distribution of perturbation energy. In contrast to an intensive direct energy cascade observed for purely vortical flows and discussed in Sec. IV, there is no apparent energy propagation to the smaller scales in Figs. 14(b), 15(b), and 16(b). Perturbation motion remains largely confined to the large scales, which strongly correlates with the absence of small scale secondary vortices, which were a signature of Kelvin–Helmholtz instability and in fact, as time progresses, there is an inverse cascade nearly back to the mean flow. Finally, we present the plots of kinetic and

potential energy of perturbations in Fig. 17. Note that intermittent behavior of perturbations for shears differs greatly from parametric instability observed for purely vortical flows. Instead, we see the perturbation amplitudes grow and peak very rapidly at $t \approx 10$ at values comparable with instability levels for vortical flows, followed by a rapid decay to the level of numerical noise at $t \approx 20$. Despite relatively large transient perturbation energy, no overturning is generated. We believe that this property is reflected in the fact that only kinetic energy amplifies strongly, while potential energy, linked directly by its definition in (19) to density perturbations, reaches only moderate values of roughly 0.5.

As a final comment we report the results of numerical simulations for shear flows at even smaller Richardson number. In this range, nonlinear stability becomes susceptible to the magnitude of initial perturbations. We discovered that the shear flow with $Ri=0.5$ was stable to perturbations with the initial energy equal to 5% of the mean flow energy. At the same time the shear flow with $Ri=0.2$ generated overturning when we perturbed it with fluctuations of the same strength. A more precise estimate of the stability threshold can be obtained by using weaker initial perturbations; however, this is not the main objective of the study described here.

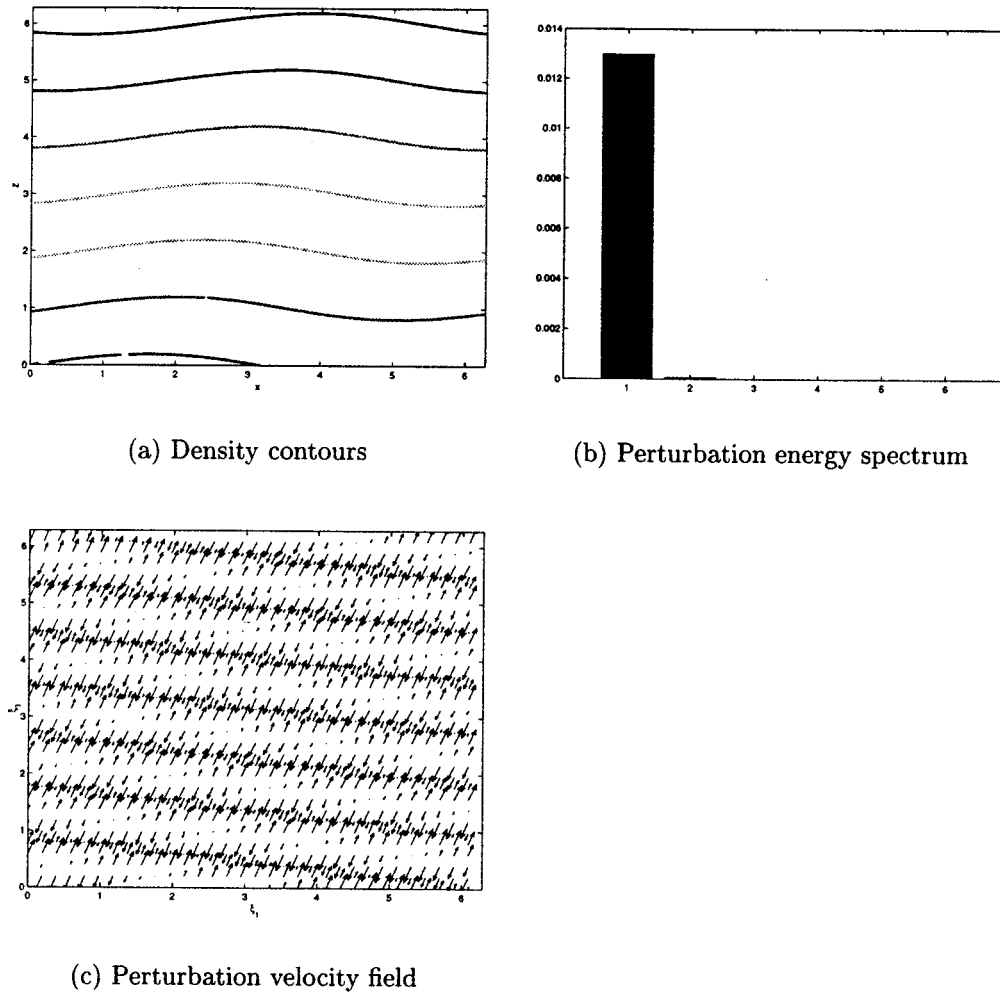


FIG. 15. As in Fig. 13, at $t=9$.

VI. FLOWS WITH VORTICITY AND SHEAR

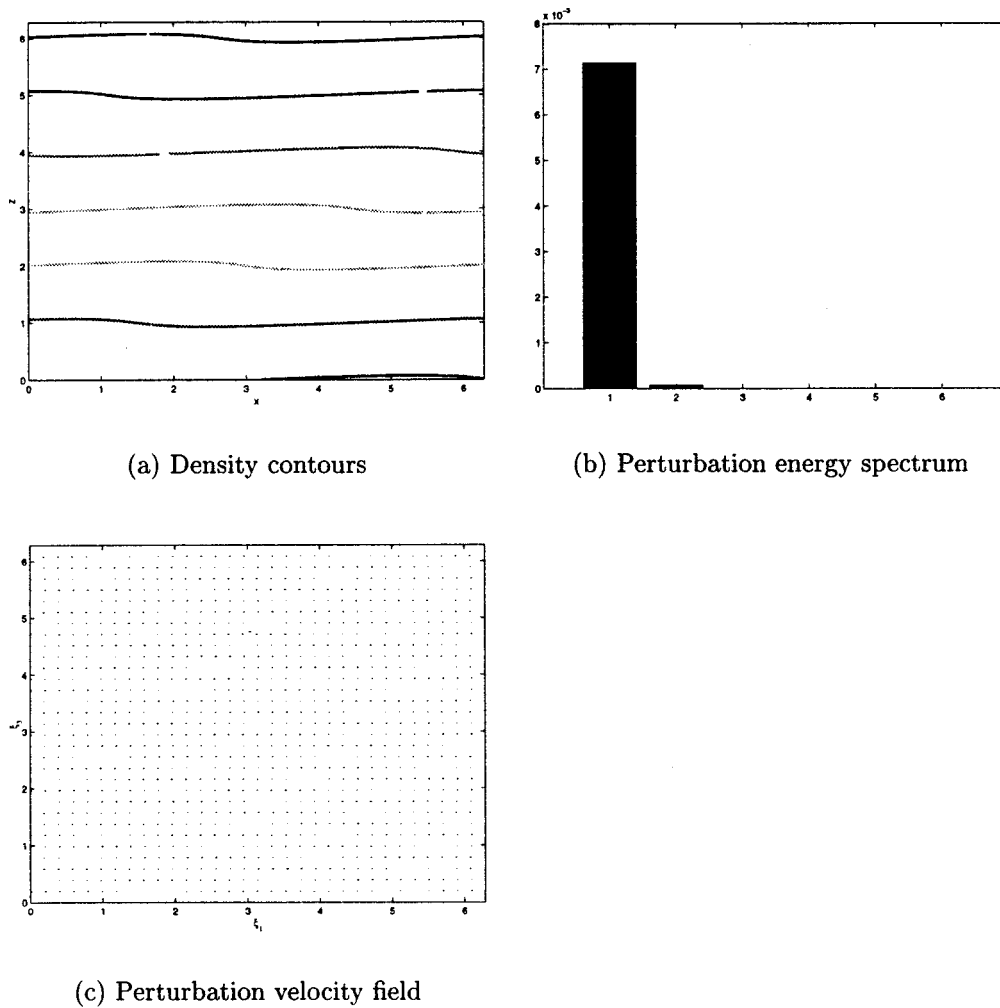
The previous two sections were devoted to the two extremal classes of elementary mean flows in two dimensions, i.e., vortical flows with no shear and shear flows with no additional rotating motion involved. In this Section we investigate the stability properties of various mean flows with combined effects of shear and vortical flows and give some quantitative thresholds for their stability and instability. We argue that stability properties are directly linked to the net shearing associated with the mean flow. A simple and efficient way to quantify the net shearing effect is to measure the effective shear, introduced in (20) and (21) from Sec. II. The effective shear reaches zero for vortical flows and coincides with the conventional shear for shear flows.

We investigated stability of a number of various mean flows parametrized by their Richardson number ($Ri = 1, 3, 5$) and the effective shear γ , ranging for each Richardson number from zero to the maximum value at the shear flow. For each flow, we directly integrated the perturbation equations in (17) with random initial data described at the beginning of Sec. IV. Figure 18 depicts each elementary flow tested by an asterisk in the (Ri, γ) plane. Purely vortical flows correspond to the lower broken line in this diagram. As we reported in Sec. IV, all vortical flows are strongly non-

linearly unstable in the wide range of Richardson numbers with significant overturning and mixing. The upper broken curve depicts shear flows; in Sec. V we verified that shears are stable in the range shown.

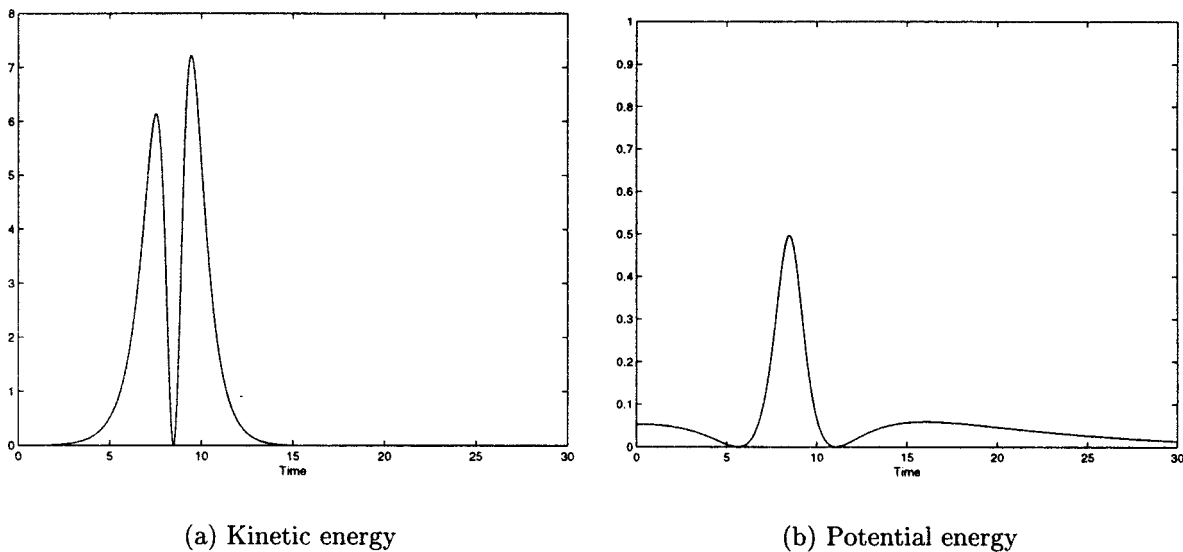
Our simulations revealed that the stability of elementary flows with fixed Richardson number is a function of the effective shear alone. The solid line in Fig. 18 schematically shows the boundary in the (Ri, γ) plane that separates flows where 10% perturbations cause overturning from nonlinearly stable flows. In particular, we found that perturbations to flows with roughly $\gamma < 0.18$ for $Ri = 1$, $\gamma < 0.1$ for $Ri = 3$ and $\gamma < 0.05$ for $Ri = 5$ generated enough density perturbations to make the overall flow overturn. We discovered that flows with the effective shear exceeding these threshold values underwent some transient amplification; however, this amplification was not sufficiently strong to overturn the flow. The properties of elementary flows with fixed Richardson number in all of our simulations varied continuously with the effective shear, with strongly overturning vortical-like behavior at small effective shears, γ , mixed behavior at intermediate γ , and stable shearlike behavior at large γ .

The occurrence of overturning events is directly related to the amplitude of perturbation potential energy, as follows from the definition in (19). To illustrate the point that only

FIG. 16. As in Fig. 13, at $t=18$.

strong enough density perturbations lead to the overturning, in Figs. 19 and 20 we show two plots of perturbation energy for the flows below and above the stability boundary for $\mathcal{R}i=1$. Indeed, we observed in the simulation with $\mathcal{R}i=1$

and $\gamma=0.07$ that perturbations develop instabilities, first aligned along the preferred direction of the linear theory, and then saturating nonlinearly to structures resembling Kelvin–Helmholtz billows with intensive overturning regions at

FIG. 17. Kinetic and potential energy of perturbation for shear flow with $\mathcal{R}i=1$.

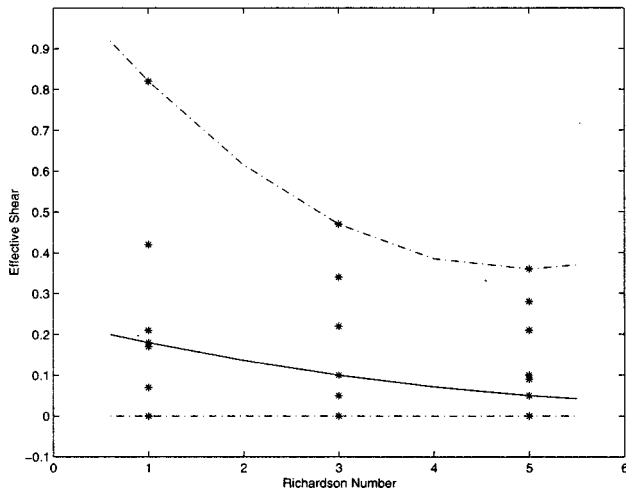


FIG. 18. Elementary flows generating overturning and flows with no overturning. Upper and lower broken lines depict shear flows and vortical flows correspondingly. Solid line shows the boundary separating elementary flows whose perturbations develop overturning instability (below the line) and stable elementary flows (above the line).

$t \approx 30$, in a fashion very similar to the one depicted in Figs. 9–11. The cascade of energy to small scales is strongly pronounced in this calculation. Figure 19 shows that the perturbation potential energy is fairly large in this simulation, reaching the magnitude 6.5 at $t \approx 40$. This example illustrates vortical-like behavior for flows with small effective shear.

On the other hand, perturbations to the flow with $Ri = 1$ and $\gamma = 0.21$, with kinetic and potential energy presented in Fig. 20, do not lead to overturning. Observe that kinetic energy reaches very high magnitudes; at $t \approx 30$ it is equal to 7, the level at which the vortical flow with the same Richardson number already overturned. The key difference with the vortical flow case, however, lies in the magnitude of potential energy. Figure 12 unambiguously shows that perturbation potential and kinetic energy for a vortical flow have comparable values at all times, with potential energy attain-

ing $O(1)$ values. In contrast to that case, the potential energy in Fig. 20 accounts for only a few percent of the total energy and has its maximum value at about 0.12, with the corresponding density perturbations too weak to cause the overturning. No direct energy cascade transfer was detected, with almost no energy allocated outside the first decade of Fourier modes at all times. This flow clearly demonstrates shearlike behavior.

To illustrate various features of the competition between vortical-like and shearlike behavior, we chose a flow located on the boundary of stability at $Ri = 3$ and $\gamma = 0.1$, where such competition of the two trends is strongly pronounced. Figures 21–23 show the characteristic density contours, regions of overturning, perturbation velocity fields and spectral distribution of the perturbation energy at times given by 4, 5.5, and 9 periods of the mean flow, which has a period equal roughly to 9, measured in buoyancy units. Again, as in Sec. V, the density contours (and the regions of overturning) are plotted in Eulerian coordinates; the velocity field has Eulerian components but is stripped of the mean flow component and mapped back into the Lagrangian frame to better visualize the structure of evolving perturbations. Figure 21 depicts an early stage of evolution, when perturbations behave similarly to the perturbations of purely vortical flows discussed in Sec. IV. We observe the formation of transient shears in the velocity field [Fig. 21(d)] aligned along the direction of fastest growth, $\alpha_0 \approx 2.9$, predicted by the linear theory and shown in Fig. 7. At a later stage, $t = 50$, we see large deviations in density contours and regions of overturning (Fig. 22). Note that a significant part of the perturbation energy cascades to the higher modes [compare Figs. 21(c) and 22(c)], which is a typical feature of perturbations for vortical flows. The structure of the velocity field [Fig. 22(c)], however, resembles a quasitraveling wave, which is a typical feature of nonlinear perturbations for shear flow perturbation. Development of the quasitraveling wave structure in the velocity field is even more apparent in Fig. 23(c), after 9 periods of the mean flow. Note that the angle of inclination

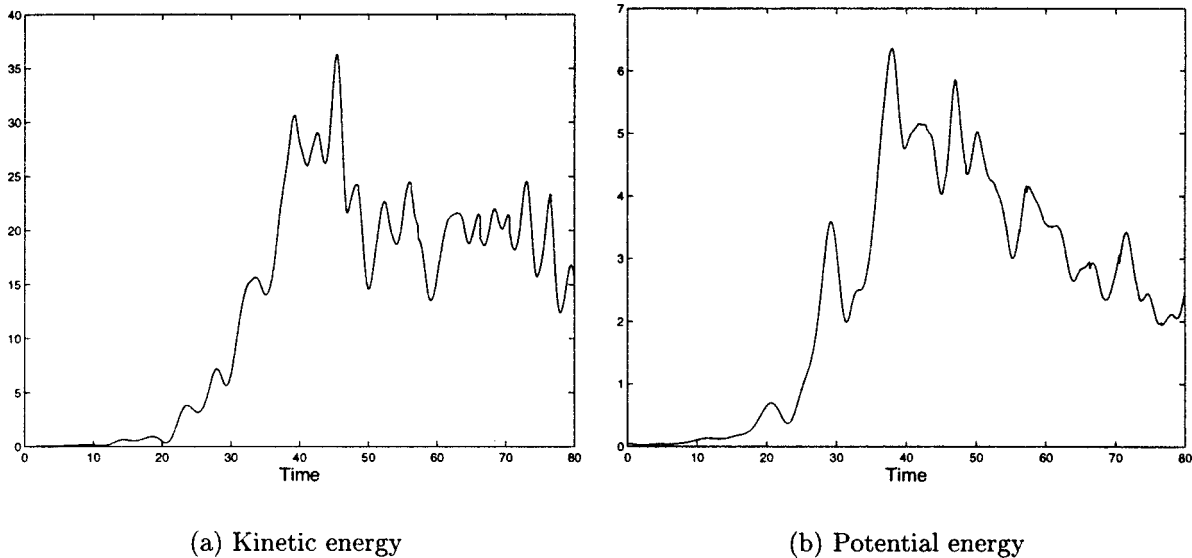
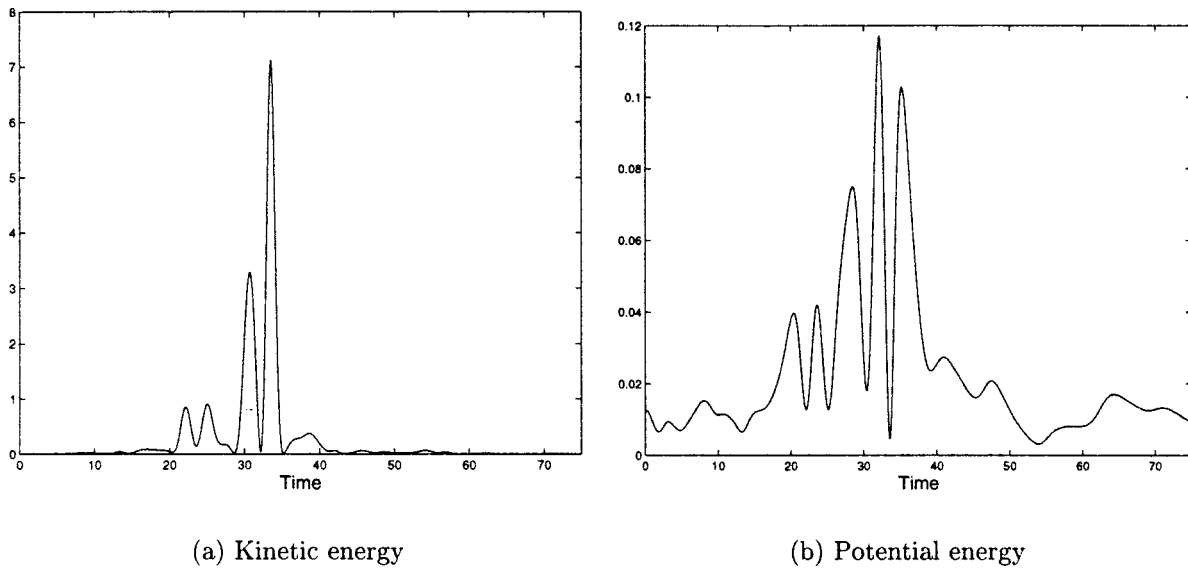
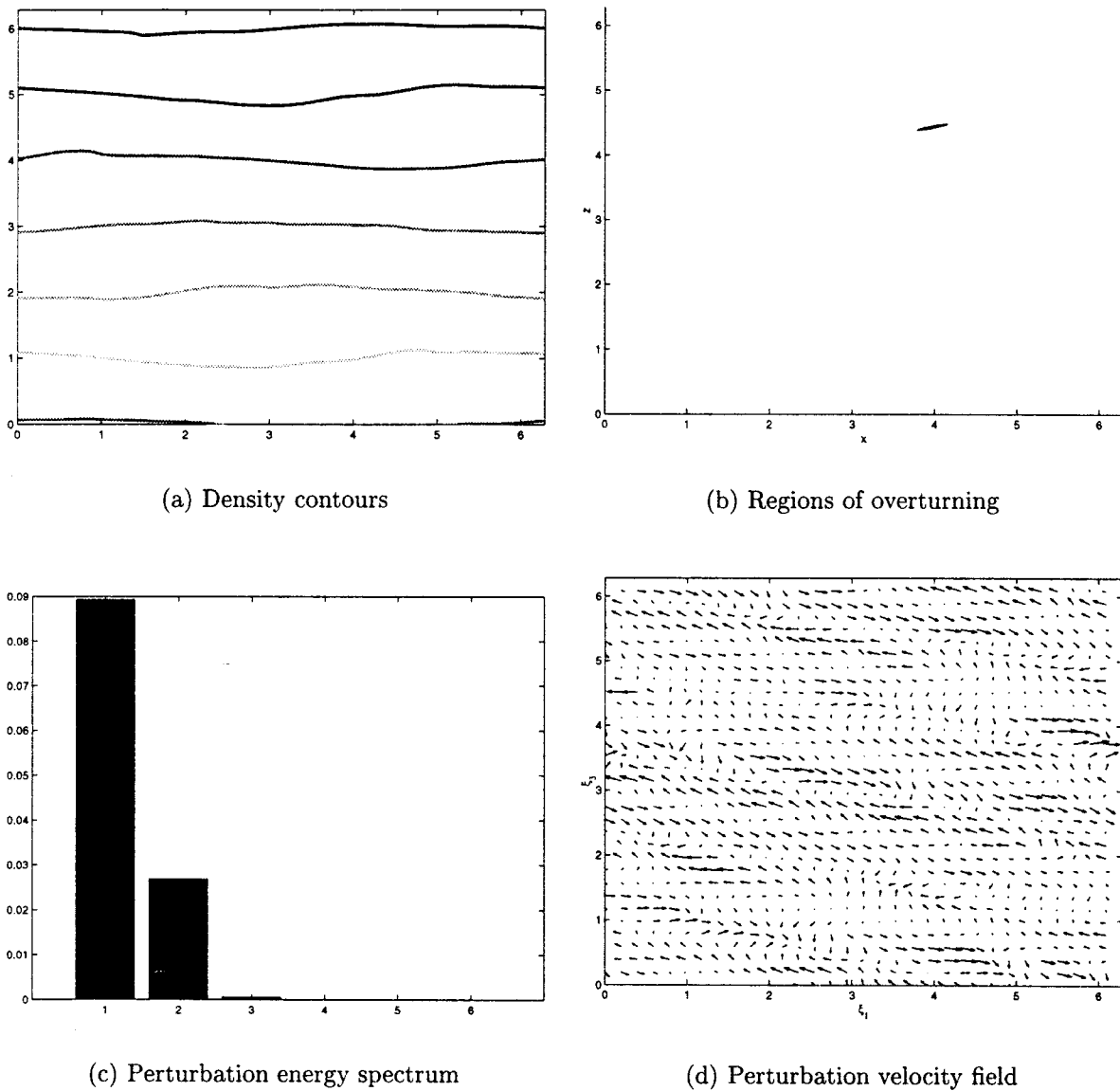
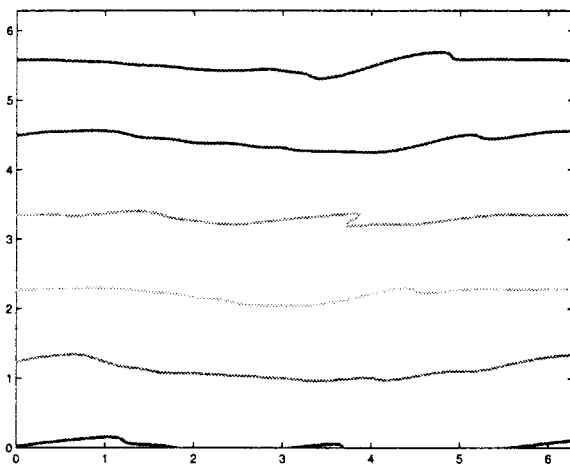
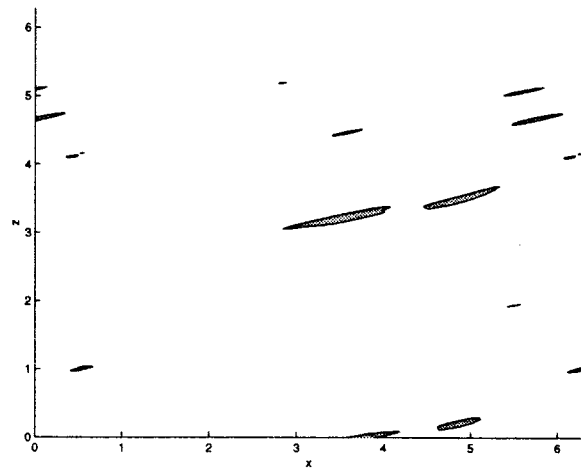


FIG. 19. Kinetic and potential energy of perturbation for flow with $Ri = 1$, $\gamma = 0.07$.

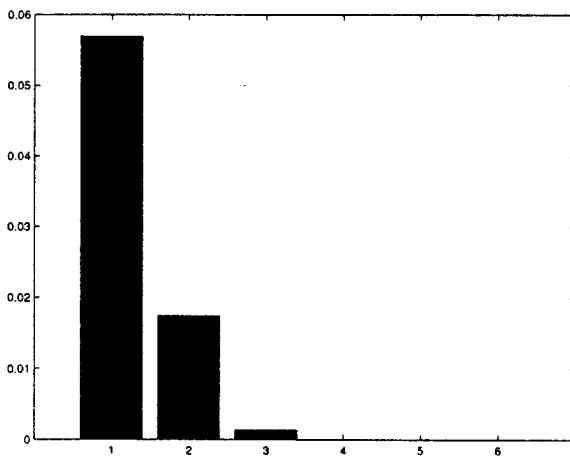
FIG. 20. Kinetic and potential energy of perturbation for flow with $Ri=1$, $\gamma=0.21$.FIG. 21. Density contours, regions of local overturning, spectral distribution of energy and velocity field of perturbation to the elementary flow with $Ri=3$, and effective shear $\gamma=0.1$ at $t=36$. Bars in the plot of spectral distribution of energy are as in Fig. 9.



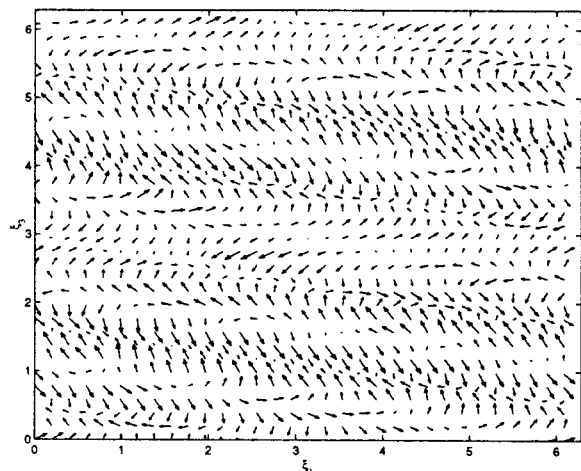
(a) Density contours



(b) Regions of overturning



(c) Perturbation energy spectrum



(d) Perturbation velocity field

FIG. 22. As for Fig. 21, at $t=59.5$.

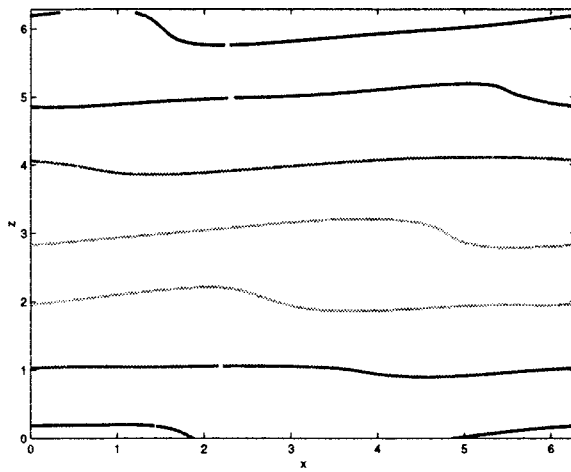
of the traveling waves fronts coincides with the fastest growth direction, as mentioned above. At large times (such as represented by Fig. 23), the flow presents no overturning regions and the energy spectrum becomes more localized at the large scales. The potential and kinetic energy for the perturbation are shown in Fig. 24. The vortical-like and shearlike stages of development are clearly distinct in these plots. For $t < 40$ kinetic and potential energy have comparable magnitude, qualitatively similar to the case of vortical flows. At longer times, the magnitude of the perturbation kinetic energy experiences oscillations with much higher amplitudes, while the potential energy associated with density perturbations remains limited; all this being a typical feature of nonlinear perturbations for a shear flow.

The case illustrated above is especially illuminating, since it combines features characteristic to both vortical and shear flows. When the effective shear falls below its critical value, flows are more vortical-like: perturbations grow and cause Kelvin–Helmholtz instability in the fashion described

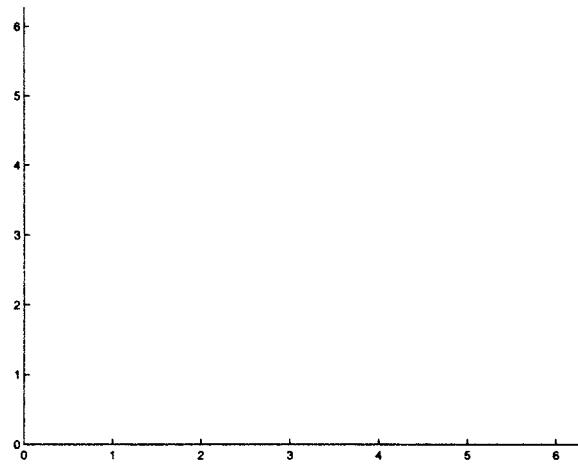
in Sec. IV. On the other hand, when the effective shear is larger than its critical value, flows are more shearlike, with no overturning and perturbation amplitudes decaying at longer times.

VII. CONCLUDING REMARKS

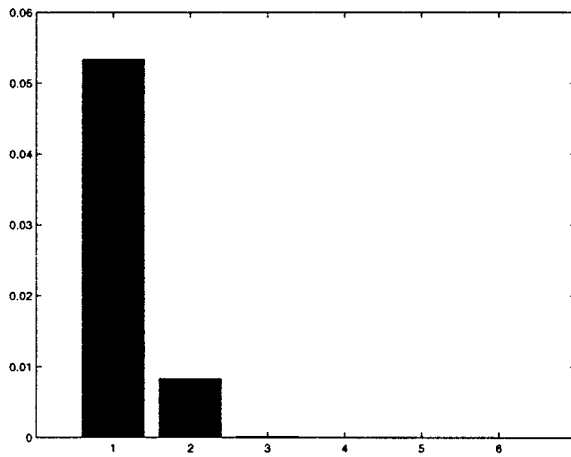
The nonlinear instability for a class of elementary stably stratified flows at large Richardson numbers has been studied here through a combination of numerical experiments and theory. The concept of effective shear has been utilized to classify the nonlinear instability in these flows. For elementary stratified flows with effective shear below a critical value depending on Richardson number, nonlinear perturbations develop strong instability with local density overturning and mixing resembling Kelvin–Helmholtz instability. Furthermore, it was established in Sec. III that these mechanisms with spontaneous generation of instability are fundamentally different from larger amplitude gravity wave break-



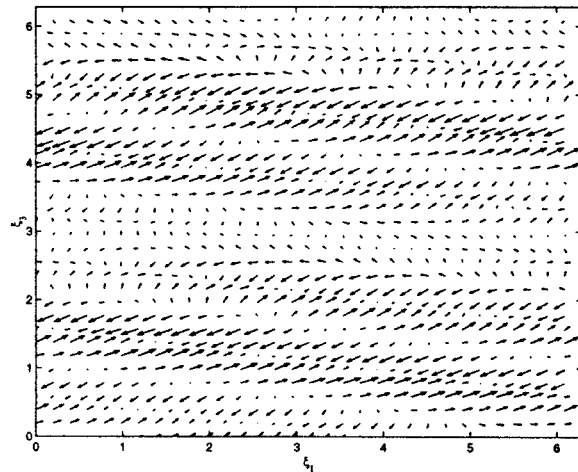
(a) Density contours



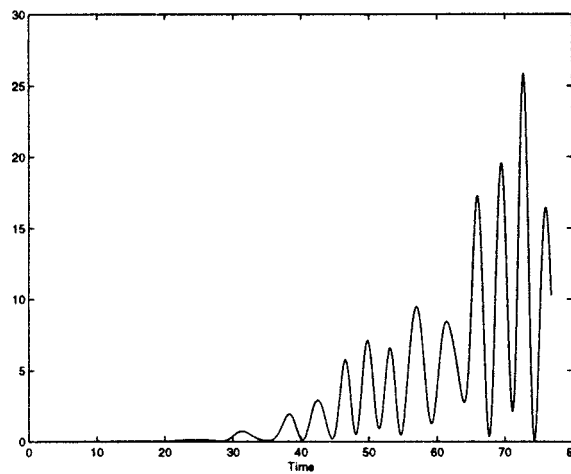
(b) Regions of overturning



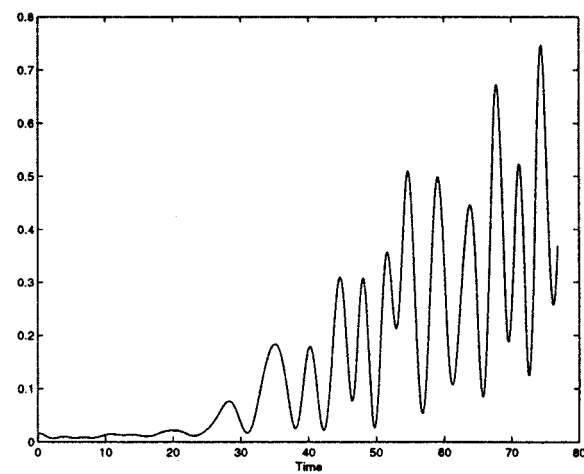
(c) Perturbation energy spectrum



(d) Perturbation velocity field

FIG. 23. As for Fig. 21, at $t=81$.

(a) Kinetic energy



(b) Potential energy

FIG. 24. Kinetic and potential energy of perturbation to elementary flow with $Ri=3$ and $\gamma=0.1$.

ing. For elementary stratified flows with effective shear above this critical value, the nonlinear development of perturbations can lead to significant growth of kinetic energy without significant transfer to the potential energy and without the overturning of density contours.

The nonlinear stability of these elementary flows has been developed here in two space dimensions where the vorticity-stream form and mean Lagrangian coordinates facilitate a more transparent analysis. As a first step, the study of nonlinear instability of such flows in two space dimensions is reasonable since the dominant linearized instabilities are purely two-dimensional.¹² To understand the robustness of the phenomena presented here and its potential physical significance, it is important to understand three-dimensional nonlinear effects as well as the role of viscosity and heat conduction. A recent Eulerian linearized stability analysis¹² yields the effect of viscosity and heat conduction for a wide range of Prandtl numbers on the linearized instabilities described here. It is an important future direction to develop numerical studies of the nonlinear saturation of such instabilities in three dimensions.

ACKNOWLEDGMENTS

Andrew J. Majda is partially supported by research Grants Nos. NSF DMS-9625795, ONR N00014-96-0043, ARO DAAG55-98-1-0129. Michael G. Shefter is supported as a post-doc by Grants Nos. NSF DMS-9625795 and ONR N00014-96-0043. The authors thank the San Diego Supercomputer Center for the opportunity to use the Cray T90 to perform high-speed computations for this work.

APPENDIX A: EQUATIONS FOR PERTURBATIONS OF PURELY VORTICAL AND SHEAR FLOWS

In this Appendix, we present simplified expressions for the Eulerian-to-Lagrangian coordinate transformation and equations in (14) for purely vortical and shear flows.

For purely vortical solutions, the mean flow parameters and coordinate transformation matrix satisfy

$$\begin{aligned}
 b_1 &= \sin \theta(t), \quad b_3 = -\cos \theta(t), \\
 \bar{\omega} &= -2 \frac{d\theta}{dt}, \quad \frac{d^2\theta}{dt^2} = -\frac{\sin \theta(t)}{2}, \\
 M_{11}(t) &= M_{22}(t) = \cos \theta(t),
 \end{aligned}
 \tag{A1}$$

$$M_{12}(t) = -M_{21}(t) = -\sin \theta(t),$$

with the initial conditions,

$$\theta(0) = 0, \quad \frac{d\theta}{dt}(0) = -\frac{Fr}{2}.$$

Note that Lagrangian particle markers trace circular orbits and return to their original positions after each period of the mean flow. The equations in (17) take the following form in this case:

$$\omega_t + (\nabla_{\xi}^{\perp} \psi \cdot \nabla_{\xi} \omega) = (\cos \theta(t) \partial_{\xi_1} - \sin \theta(t) \partial_{\xi_3}) \rho,$$

$$\rho_t + (\nabla_{\xi}^{\perp} \psi \cdot \nabla_{\xi} \rho) = -\frac{\partial \psi}{\partial \xi_1}, \tag{A3}$$

$$\Delta_{\xi} \psi = \omega.$$

Next, we derive similar formulas for shear flows. Recall that shear flows are the equilibrium solutions, with the mean flow parameters $\bar{\omega}, b_1, b_3$ constant in time and given by their initial conditions, as stated in (13). An easy check shows that the components of the coordinate transformation map between the Eulerian and Lagrangian frames comprise a ‘‘shearing’’ matrix, $M(t)$,

$$M_{11}(t) \equiv 1, \quad M_{12} = \bar{\omega}_0 t, \quad M_{21} \equiv 0, \quad M_{22} \equiv 1.$$

The Lagrangian particle markers in this case are transported horizontally by the mean flow, with the speed proportional to their vertical coordinate, so that the equations in (17) assume the form,

$$\omega_t + (\nabla_{\xi}^{\perp} \psi \cdot \nabla_{\xi} \omega) = \rho_{\xi_1},$$

$$\rho_t + (\nabla_{\xi}^{\perp} \psi \cdot \nabla_{\xi} \rho) = -\psi_{\xi_1}, \tag{A4}$$

$$((\bar{\omega}_0^2 t^2 + 1) \partial_{\xi_1 \xi_1}^2 + \partial_{\xi_3 \xi_3}^2 - 2 \bar{\omega}_0 t \partial_{\xi_1 \xi_3}^2) \psi = \omega.$$

APPENDIX B: LINEAR STABILITY ANALYSIS IN LAGRANGIAN AND EULERIAN FRAMES

In this paper we make an extensive use of mean Lagrangian coordinates that are associated with the particles, following the unperturbed trajectories of liquid particles of exact elementary solutions discussed in Sec. II. The equations for wavelike perturbations in (14) have a simplified form in these coordinates. However, to complete the study and to justify the connection with the earlier results obtained in Eulerian coordinates, we will show that the equations in (17) are equivalent to the equations describing evolution of two-dimensional wavelike perturbations in Eulerian coordinates,

$$u(x, z, t) = A_1(t) F(\alpha_1(t)x + \alpha_3(t)z + \phi_0),$$

$$w(x, z, t) = A_3(t) F(\alpha_1(t)x + \alpha_3(t)z + \phi_0),$$

$$\rho(x, z, t) = B(t) F(\alpha_1(t)x + \alpha_3(t)z + \phi_0).$$

Here, $\vec{v} = (u(x, z, t), w(x, z, t))$ and $\rho(x, z, t)$ is the two-dimensional perturbation field, $\vec{a}(t)$ is the time-dependent wave vector in Eulerian coordinates and ϕ_0 is an arbitrary phase shift. These variables satisfy the following equations:¹²

$$\begin{aligned}\frac{d\alpha_1}{dt} &= \frac{\bar{\omega}(t) - \sigma}{2} \alpha_3, \\ \frac{d\alpha_3}{dt} &= -\frac{\bar{\omega}(t) + \sigma}{2} \alpha_1, \\ \frac{dA_1}{dt} &= -\frac{\bar{\omega}(t) + \sigma}{2} A_3 + \frac{\alpha_1}{|\vec{\alpha}|^2} (A_1 \alpha_3 (\sigma - \bar{\omega}(t))) \\ &\quad + A_3 \alpha_1 (\sigma + \bar{\omega}(t)) + \frac{\alpha_1 \alpha_3}{|\vec{\alpha}|^2} B, \end{aligned} \quad (\text{B1})$$

$$\begin{aligned}\frac{dA_3}{dt} &= \frac{\bar{\omega}(t) - \sigma}{2} A_1 + \frac{\alpha_3}{|\vec{\alpha}|^2} (A_1 \alpha_3 (\sigma - \bar{\omega})) \\ &\quad + A_3 \alpha_1 (\sigma + \bar{\omega}(t)) + \left(\frac{\alpha_3^2}{|\vec{\alpha}|^2} - 1 \right) B, \\ \frac{dB}{dt} &= -A_1 b_1 - A_3 b_3, \end{aligned}$$

with the mean flow parameters, $\bar{\omega}(t), b_1(t), b_3(t)$ defined in (5) and evolving according to (6). From the identity

$$(\vec{k} \cdot \vec{\xi}) = (\vec{k} \cdot M^{-1}(t) \vec{x}) = ((M^{-1}(t))^T \vec{k} \cdot \vec{x}) = (\vec{\alpha}(t) \cdot \vec{x}),$$

we obtain the relationship between Eulerian and Lagrangian wave vectors,

$$\vec{\alpha}(t) = (M^{-1}(t))^T \vec{k}, \quad \vec{k} = M(t)^T \vec{\alpha}(t). \quad (\text{B2})$$

Using the incompressibility condition, $\det M(t) = 1$, we rewrite the transformation formulas above in the explicit form,

$$\begin{aligned}\vec{\alpha}(t) &= \begin{pmatrix} M_{22}(t) & -M_{21}(t) \\ -M_{12}(t) & M_{11}(t) \end{pmatrix} \vec{k}, \\ \vec{k} &= \begin{pmatrix} M_{11}(t) & M_{21}(t) \\ M_{12}(t) & M_{22}(t) \end{pmatrix} \vec{\alpha}(t). \end{aligned}$$

Direct evaluation of $d\vec{\alpha}(t)/dt$, with the derivatives of transformation matrix $M(t)$ computed according to (16), leads to

$$\begin{aligned}\frac{d\vec{\alpha}}{dt} &= \begin{pmatrix} \frac{-\bar{\omega}(t) + \sigma}{2} M_{12}(t) & \frac{\bar{\omega}(t) - \sigma}{2} M_{11}(t) \\ -\frac{\bar{\omega}(t) + \sigma}{2} M_{22}(t) & \frac{\bar{\omega}(t) + \sigma}{2} M_{21}(t) \end{pmatrix} \vec{k} \\ &= \begin{pmatrix} \frac{\bar{\omega}(t) - \sigma}{2} \alpha_3 \\ -\frac{\bar{\omega}(t) + \sigma}{2} \alpha_1 \end{pmatrix}. \end{aligned}$$

The last expression recovers the first two equations in (B1) that describe the evolution of Eulerian wave vector. Next, we use the incompressibility constraint, $(M_{11}(t)M_{22}(t) - M_{12}(t)M_{21}(t)) \equiv 1$, and the fact that \hat{L}_k^{-1} in (24) transforms into $-1/|\vec{\alpha}|^2$, to rewrite the equations in (23), using Eulerian the wave vector $\vec{\alpha}(t)$,

$$\frac{d\hat{\omega}_k}{dt} = -\alpha_1(t) \hat{\rho}_k(t), \quad (\text{B3})$$

$$\frac{d\hat{\rho}_k}{dt} = \frac{M_{11}(t)\alpha_1(t) + M_{21}(t)\alpha_3(t)}{|\vec{\alpha}(t)|^2} \hat{\omega}_k(t).$$

In the context of plane waves, $\hat{\omega}_k(t)$ is obviously related to the velocity components A_1 and A_3 via

$$\hat{\omega}_k(t) = -A_1(t)\alpha_3(t) + A_3(t)\alpha_1(t).$$

Here and everywhere else, \vec{k} is related to $\vec{\alpha}(t)$ via (B2). After taking a derivative of the expression above, we use the equations in (B1) and the incompressibility condition $\vec{A}(t) \cdot \vec{\alpha}(t) \equiv 0$ to arrive at the first equation in (B3).

A simple check confirms that the perturbation velocity components can be expressed in terms of the perturbation vorticity,

$$A_1 = -\alpha_3(t) \frac{\hat{\omega}_k(t)}{|\vec{\alpha}(t)|^2}, \quad A_3 = \alpha_1(t) \frac{\hat{\omega}_k(t)}{|\vec{\alpha}(t)|^2}.$$

The last equation in (B1) then assumes the form

$$\begin{aligned}B_t &= -b_1(t)A_1(t) - b_3(t)A_3(t) \\ &= (\alpha_3(t)b_1(t) - \alpha_1(t)b_3(t)) \frac{\hat{\omega}_k(t)}{|\vec{\alpha}(t)|^2}. \end{aligned} \quad (\text{B4})$$

At the end of Sec. IIC we showed that $M_{21}(t) \equiv b_1(t)$ and $M_{11}(t) \equiv -b_3(t)$. With this observation, (B4) recovers completely the second equation in (B3); this completes the proof of the equivalence between Eulerian and Lagrangian formulations.

¹H. J. S. Fernando, "Turbulent mixing in stratified fluids," *Annu. Rev. Fluid Mech.* **23**, 455–493 (1991).

²H. J. S. Fernando and J. C. R. Hunt, "Some aspects of turbulence and mixing in stably stratified layers," *Dyn. Atmos. Oceans* **23**, 35–62 (1996).

³C. S. Bretherton *et al.*, "An intercomparison of radiatively-driven entrainment and turbulence in a smoke cloud, as simulated by different numerical models," *Q.J.R. Meteorol. Soc.* (in press).

⁴D. A. Siegel and J. A. Domaradzki, "Large-Eddy simulation of decaying stably stratified turbulence," *J. Phys. Oceanogr.* **24**, 2353–2385 (1994).

⁵J. W. Miles, "On the stability of heterogeneous shear flows," *J. Fluid Mech.* **10**, 496–508 (1961).

⁶L. N. Howard, "Note on a paper of John W. Miles," *J. Fluid Mech.* **13**, 158–160 (1961).

⁷D. K. Lilly, "The representation of small-scale turbulence in numerical simulation experiments," in *Proceedings of the IBM Scientific Computing Symposium on Environmental Science*, pp. 195–210, 1967.

⁸J. Smagorinsky, "General circulation experiments with the primitive equations. I. The basic experiment," *Mon. Weather Rev.* **91**, 99–164 (1963).

⁹J. W. Lavelle and D. C. Smith, "Effects of rotation on convective plumes from line segment source," *J. Phys. Oceanogr.* **26**, 863–872 (1996).

¹⁰P. G. Drazin, "On the instability of an internal gravity wave," *Proc. R. Soc. London, Ser. A* **356**, 411–432 (1977).

¹¹P. N. Lombard and J. J. Riley, "On the breakdown into turbulence of propagating internal waves," *Dyn. Atmos. Oceans* **23**, 345–355 (1996).

¹²A. J. Majda and M. G. Shefter, "Elementary stratified flows with instability at large Richardson number," *J. Fluid Mech.* **376**, 319–350 (1998).

¹³I. Orlandi, "Trapeze instability as a source of internal gravity waves. Part I," *J. Atmos. Sci.* **54**, 577–598 (1997).

¹⁴A. D. D. Craik and W. O. Criminalle, "Evolution of wavelike disturbances in shear flows: a class of exact solutions of the Navier-Stokes equations," *Proc. R. Soc. London, Ser. A* **406**, 13–26 (1986).

¹⁵A. J. Majda, "Vorticity and the mathematical theory of incompressible flow," *Commun. Pure Appl. Math.* **39**, 5187–5209 (1986).

- ¹⁶W. E and C. Shu, "Small-scale structures in Boussinesq convection," *Phys. Fluids* **6**, 49–58 (1994).
- ¹⁷W. O. Criminale and J. Q. Cordova, "Effects of diffusion in the asymptotics of perturbations in stratified shear flow," *Phys. Fluids* **29**, 2054–2060 (1986).
- ¹⁸B. F. Farrell and P. J. Ioannou, "Transient development of perturbations in stratified shear flow," *J. Atmos. Sci.* **50**, 2201–2214 (1993).
- ¹⁹G. P. Klaassen and W. R. Peltier, "Evolution of finite amplitude Kelvin-Helmholtz billows in two spatial dimensions," *J. Atmos. Sci.* **42**, 1321–1339 (1985).
- ²⁰A. J. Majda and M. G. Shefter, "The instability of stratified flows at large Richardson numbers," *Proc. Natl. Acad. Sci. USA* **95**, 7850–7853 (1998).